

RESEARCH ARTICLE | MAY 26 2023

## Quantifying the effects of dissolved nitrogen and carbon dioxide on drying pressure of hydrophobic nanopores

Special Collection: [Chemical Physics of Controlled Wettability and Super Surfaces](#)

Hikmat Binyaminov ; Janet A. W. Elliott  

 Check for updates

*J. Chem. Phys.* 158, 204710 (2023)

<https://doi.org/10.1063/5.0146952>



View  
Online



Export  
Citation

CrossMark

500 kHz or 8.5 GHz?  
And all the ranges in between.

Lock-in Amplifiers for your periodic signal measurements



Find out more

 Zurich  
Instruments

# Quantifying the effects of dissolved nitrogen and carbon dioxide on drying pressure of hydrophobic nanopores

Cite as: *J. Chem. Phys.* **158**, 204710 (2023); doi: [10.1063/5.0146952](https://doi.org/10.1063/5.0146952)

Submitted: 17 February 2023 • Accepted: 20 April 2023 •

Published Online: 26 May 2023



View Online



Export Citation



CrossMark

Hikmat Binyaminov  and Janet A. W. Elliott<sup>a)</sup> 

## AFFILIATIONS

Department of Chemical and Materials Engineering, University of Alberta, Edmonton, Alberta T6G 1H9, Canada

**Note:** This paper is part of the JCP Special Topic on Chemical Physics of Controlled Wettability and Super Surfaces.

<sup>a)</sup> Author to whom correspondence should be addressed: [janet.elliott@ualberta.ca](mailto:janet.elliott@ualberta.ca)

## ABSTRACT

The effects of a dissolved gas on the behavior of liquid in cylindrical nanopores are investigated in the framework of Gibbsian composite system thermodynamics and classical nucleation theory. An equation is derived relating the phase equilibrium of a mixture of a subcritical solvent and a supercritical gas to the curvature of the liquid–vapor interface. Both the liquid and the vapor phases are treated nonideally, which is shown to be important for the accuracy of the predictions in the case of water with dissolved nitrogen or carbon dioxide. The behavior of water in nanoconfinement is found to be only affected when the gas amount is significantly more than the saturation concentration of these gases at atmospheric conditions. However, such concentrations can be easily reached at high pressures during intrusion if there is sufficient gas present in the system, especially considering gas oversolubility in confinement. By including an adjustable line tension term in the free energy equation ( $-44$  pJ/m for all points), the theory can make predictions in line with the few data points available from recent experimental work. However, we note that such a fitted value empirically accounts for multiple effects and should not be interpreted as the energy of the three-phase contact line. Compared to molecular dynamics simulations, our method is easy to implement, requires minimal computational resources, and is not limited to small pore sizes and/or short simulation times. It provides an efficient path for first-order estimation of the metastability limit of water–gas solutions in nanopores.

Published under an exclusive license by AIP Publishing. <https://doi.org/10.1063/5.0146952>

## I. INTRODUCTION

The dynamics of intrusion and extrusion of liquids into and out of nanoscale environments have drawn great interest in recent years, owing mainly to the increasing number of technological and industrial applications, such as fluid separation,<sup>1</sup> energy dampening and storage,<sup>2–5</sup> porosimetry,<sup>6</sup> and DNA sequencing,<sup>7</sup> among many others. The interplay of the parameters that dictate the behavior of a liquid in confinement is notoriously difficult to determine, leading to poor predictability, controllability, and other design challenges.<sup>8,9</sup> Additionally, understanding of these processes is crucial from a fundamental science perspective as they are believed to play an important role in many organic phenomena, such as gating in biological channels.<sup>10–14</sup>

One of the variables that strongly affects the characteristics of a liquid in confinement is the dissolved gas, such as nitrogen,

which is naturally present in the liquid, such as water, if special precautions are not taken to eliminate it.<sup>15,16</sup> The ability of the dissolved gas to promote the drying of a liquid-filled pore has implications beyond technological applications. For example, in biology, the anesthetic potency of a gas is known to be related to its solubility<sup>17</sup> (the Meyer–Overton correlation). Although the phenomenon has been known for over a century, and many hypotheses have been put forward to explain it since, a scientific consensus has not yet been reached. In recent years, a new idea has been gaining popularity with growing evidence suggesting a mechanism where the gas migrates to the channels of the lipid bilayer, destabilizes the liquid, and creates a vapor bubble that blocks the ion transfer.<sup>11,14,18</sup>

Previously, equilibrium density functional theory<sup>11</sup> and molecular dynamics simulations<sup>18–23</sup> have been utilized to study the effects of a weakly soluble gas on the wet-to-dry transition in nanoconfinement. Roth *et al.*<sup>11</sup> studied gating in a model hydrophobic biological

channel. Their calculations show that a small amount of xenon gas dramatically decreases the open probability of a channel with a radius in the 0.4–1.2 nm range. In the molecular dynamics simulations of Camisasca *et al.*,<sup>18</sup> a single atom of argon gas was able to migrate into a water-filled nanopore with a radius of 0.7 nm and result in the drying of the pore within the simulation time by reducing the free energy barrier considerably and nucleating a bubble. By means of molecular dynamics simulations, Li *et al.*<sup>22</sup> studied the effect of nitrogen gas on the critical distance between hydrophobic plates in water. They concluded that, by aggregating near the surfaces of the plates, the gas increases the critical distance below which water is unstable in the confinement. In a similar study by Feng *et al.*,<sup>24</sup> an electric field applied perpendicularly to the plates resulted in enhanced aggregation of the nitrogen molecules in the slit and further increased the critical distance in proportion to the field strength. Leung *et al.*<sup>23</sup> realized that, at atmospheric pressures, the dissolved gases should have no significant effect on drying by performing simulations with water confined in hydrocarbon-like slits. In their simulations, a single nitrogen molecule inserted into the slit reduced the free energy barrier by  $\sim 2k_B T$ , where  $k_B$  is the Boltzmann constant and  $T$  is the absolute temperature. Luzar and Bratko<sup>19</sup> found that the fugacities of nitrogen and carbon dioxide required to trigger the expulsion of water from a 1.4 nm narrow hydrophobic slit were  $\sim 40$  and  $\sim 2$  bars, respectively.

There have been some experimental attempts<sup>20,25–27</sup> to quantify the effects of dissolved gases on the behavior of water in nanoconfinement. Li *et al.*<sup>25,27</sup> used nanoporous material with cylindrical pores of varying sizes mixed with water and conducted experiments with different amounts of air in the system. At the end of the first compression–decompression cycle, depending on the amount of gas, very little, some, or most of the total nanopore volume could be recovered for use in the second cycle. In the works of Xu *et al.*<sup>26</sup> and Qiao *et al.*,<sup>20</sup> the researchers performed experiments with cylindrical nanopores open at both ends and closed at one end, respectively, with trapped gas occupying the pore volume at the beginning of intrusion (i.e., air; the samples were not degassed). Both groups observed that if the samples were held at high pressures at the end of the infiltration process ( $\sim 3$  to 12 h holding time), a significant portion of the useable nanopore volume was lost in the next cycle. On the other hand, if the intrusion and extrusion processes were performed in succession with no holding, all pore volume was recovered, allowing practically identical intrusion–extrusion cycles. This was because the trapped gas in the nanopores was not enough to saturate the liquid at the pressure at which the samples were held, and gas was diffusing into the bulk liquid (a rather slow process), reducing the gas concentration in the pores. No drying was observed in the same experiment by Qiao *et al.*,<sup>20</sup> performed with material with a larger average pore size, regardless of the presence of gas or high-pressure holding.

In this work, we study the effect of dissolved nitrogen and carbon dioxide on the wet/dry state of a cylindrical nanopore in the framework of Gibbsian composite system thermodynamics coupled with classical nucleation theory. Previously, using similar methods, our group explored free energy landscapes in other geometries, such as the formation of bubbles in finite cones<sup>28</sup> or the stability of surface nanobubbles.<sup>29</sup> In these works, the pressures considered were low enough that the ideal mixture assumptions could be safely made. We have also developed equations for liquid–vapor equi-

librium of multicomponent mixtures of condensable components accounting for the effect of interfacial curvature and the liquid phase nonideality.<sup>30,31</sup> The extension to the nonideal vapor phase was mentioned in Ref. 32 but not applied. Here, to study the stability of water in cylindrical nanopores in the presence of gas, we derive the fully nonideal phase equilibrium equations for a mixture of a condensable solvent and a noncondensable gas with a curved liquid–vapor interface. These equations can be applied to any confinement geometry and interface shape and are accurate for typical pressures of interest in the study of liquids in nanopores.

Regarding the applicability of the macroscopic thermodynamic equations at extreme confinement and the reliability of the predictions, there are many works in the literature supporting their validity under certain circumstances in the 1–4 nm size range.<sup>33</sup> For instance, it has been shown that the macroscopic equation relating the saturation vapor pressure of the liquid to the curvature of the interface—the Kelvin equation—holds for clusters as small as 0.7 nm in radius.<sup>34</sup> In our group's previous work, the multicomponent version of this equation applied to pores of 2 nm radius gave predictions of composition-dependent dew points of subcritical mixtures in excellent agreement with independent measurements.<sup>31</sup> Another example is the Young–Laplace equation (in fact, it is used in the derivation of the Kelvin equation), which has been demonstrated to be valid for nanodroplets down to radii of 1 nm.<sup>35</sup> In the context of nanopores, this equation is known to accurately predict the intrusion pressures for pore radii of 1.3 nm and larger.<sup>15,16,36,37</sup> Additionally, it has been concluded that the properties of water bridges sandwiched between two planar surfaces can be calculated using capillary theory for wall separations of 3 nm and above with no additional corrections.<sup>38</sup> Moreover, classical nucleation theory with the Kelvin equation applied to the nitrogen–ethyl ether mixture was able to accurately predict the homogeneous bubble nucleation rate and correctly capture its pressure and temperature dependencies.<sup>39,40</sup>

## II. SYSTEM DEFINITION AND FREE ENERGY

A schematic description of the system is given in Fig. 1. We consider a piston–cylinder device that is coupled with a constant pressure ( $P^R$ ) and constant temperature ( $T^R$ ) reservoir with which only volume and energy exchanges are allowed. We let the system exist in the absence of external forces, such as gravity. We assume that the container is filled with a liquid with dissolved gas in it, which is denoted by the superscript letter “L” (referred to as “liquid” or “solution”). Sufficient for the analysis here, we consider a single cylindrical pore open at both ends with an internal radius of  $R_p$  and a length of  $l_p$  placed in the liquid. It is assumed that the pore is made of a solid material with which the liquid would have a macroscopic equilibrium contact angle  $\theta_{eq}$  (measured through the liquid) if placed on a flat surface. The solid is taken to be insoluble, nonvolatile, and infinitely rigid.

After the pore is filled with the liquid, the pressure is suddenly brought to pressure  $P_{ext} = P^R$ , which is referred to as the extrusion pressure. This is the pressure at which the pore empties (or dries) in an experiment in a reasonable time. A schematic of the system immediately after the pressure is brought to  $P_{ext}$  is given in Fig. 1(a). As depicted in Fig. 1(b), after a short time, the liquid starts to empty the pore while the piston moves up to

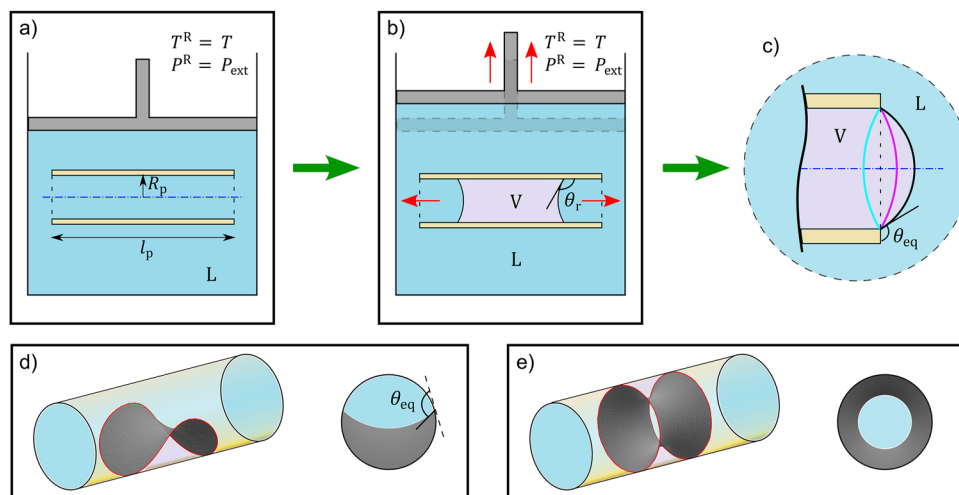


**FIG. 1.** Schematic description of the drying of a cylindrical nanopore immersed in a liquid–gas solution. The metastable reference state is shown in panel (a) with a solution-filled cylinder of radius  $R_p$  and length  $l_p$ . After a short waiting time, a new vapor phase forms and pushes the solution out of the pore following a nucleation event. Schematics of possible critical nucleus geometries considered in this work are depicted in panels (d) (localized nucleus) and (e) (symmetric nucleus). A snapshot of the process after the nucleation is shown in panel (b), where two disjoint spherical caps are moving in opposite directions. The final equilibrium state with the vapor-filled pore and a pinned liquid–vapor interface covering the pore mouth at the end of this process is depicted in panel (c). In this panel, the light blue, purple, and black lines indicate example positions of the interface, depending on the pressure difference,  $P^V - P^L$ . The liquid–gas solution is indicated by the letter “L,” and the vapor is indicated by the letter “V.” The liquid has an equilibrium contact angle of  $\theta_{eq}$  with the solid. While the interface is in motion, the contact angle,  $\theta_r$ , in general, is assumed to be different than  $\theta_{eq}$ . Note that  $\theta_r$  does not appear in our calculations because we are only concerned with equilibrium states in this work.

accommodate the formation of the new vapor phase in the pore, which is denoted by “V” (referred to as “vapor”). Finally, the system reaches a new equilibrium state where the pore is sealed at both ends with pinned spherical liquid–vapor interfaces, as depicted in Fig. 1(c). We note that the final pinned equilibrium state is only possible if the difference between the vapor phase pressure and the liquid phase pressure,  $\Delta P = P^V - P^L$ , is not larger than the pore mouth geometry can accommodate. This threshold pressure difference is denoted by  $\Delta P^*$ . Assuming a flat pore mouth surface, it can be calculated as  $\Delta P^* = 2\sigma^{LV} \sin \theta_{eq}/R_p$ , where  $\sigma^{LV}$  is the surface tension of the liquid–vapor interface. This means that the inequality  $\Delta P \leq \Delta P^*$  should be satisfied for the vapor phase to stay confined in the pore.

It has been experimentally confirmed<sup>15,16,36,37</sup> that the capillary pressure required to force the liquid into an initially dry pore (initially, the pressure is zero inside the capillary) is well described by Laplace’s law of capillarity,

$$P_{int} = -\frac{2\sigma^{LV} \cos \theta_a}{R_p}, \quad (1)$$

where  $P_{int}$  is the required intrusion pressure and  $\theta_a \geq \theta_{eq}$  is the advancing contact angle. Notice that a positive intrusion pressure is required if the solid is nonwetting (i.e., if  $\theta_{eq} > 90^\circ$ ).

In our analysis, the intrusion pressure  $P_{int}$  only serves as a guide for the concentration of the gas in the liquid, which can be independently set to make the liquid (i) undersaturated, (ii) saturated, or (iii) oversaturated with respect to  $P_{int}$ . The most obvious case would be to assume that the concentration of the gas in the liquid

after the system pressure is brought to  $P_{ext}$  is equal to the saturation concentration of the gas at  $P_{int}$ . However, other possibilities are also considered to gain insight into the physics of the problem. In practice, undersaturation may happen due to, for example, not having enough gas molecules in the system for saturation, and oversaturation can be the result of the initial pressure being higher than the required (minimum) intrusion pressure,  $P_{int}$ , in an abundance of gas. In experiments, one usually deals with many pores in one system with a certain pore size distribution. As a result, the maximum pressure reached for the complete intrusion of all pores can be significantly higher (typically at least ~30% to 50% higher) than the mean intrusion pressure. If the pore studied in this work represents the average pore size in the experiments, it is reasonable to consider oversaturation with respect to the required intrusion pressure. Furthermore, nanopores are known to attract “hydrophobic” dissolved gas resulting in a significant increase in gas concentrations in the pore compared to the bulk concentration.<sup>19,41–47</sup>

In the experiments, the extrusion pressure is often measured to be significantly lower than the required intrusion pressure while (linearly) increasing with temperature, indicating that there exists a free energy barrier that needs to be overcome. This energy barrier is associated with the formation of a critical nucleus of vapor (which contains both vapor of the solvent and gas) because of random fluctuations in the liquid, as formulated in the context of classical nucleation theory.<sup>48</sup> This nucleus is in an unstable equilibrium with the liquid, and as a result, smaller nuclei disappear, and larger nuclei grow until a new equilibrium state is reached. It is well known that heterogeneous bubble nucleation (i.e., creation of a nucleus in contact with the pore wall) has a lower energy barrier compared to

homogeneous bubble nucleation (i.e., creation of a nucleus in the bulk liquid inside the pore), especially when  $\theta_{\text{eq}} > 90^\circ$ .<sup>48</sup> Therefore, only the formation of a critical nucleus on the pore wall (inside the pore) is considered. The shape of this nucleus will be discussed later, as it may have nontrivial geometry due to the confinement inside the cylinder. The nucleus shape need not be specified for the derivation and qualitative description of the thermodynamic potential of the system (the free energy equation).

To investigate the nature of equilibrium states, it suffices to study the free energy equation in the neighborhood of an equilibrium state. Following the standard techniques,<sup>32,39,49–52</sup> the expansion of the free energy in intensive parameters around the equilibrium state can be written. Because the variations around equilibrium can be made arbitrarily small, only the first order terms can be retained, which reduces to<sup>52</sup>

$$\Delta B(V^V) = -V^V \sigma^{\text{LV}} k_c + \sigma^{\text{LV}} A^{\text{LV}} + \sigma^{\text{LV}} A^{\text{SV}} \cos \theta_{\text{eq}}, \quad (2)$$

where  $B$  is the free energy function,  $V^V$  is the volume of a nucleus, and  $k_c = 1/R_{1,c} + 1/R_{2,c}$  is twice the mean curvature of the liquid–vapor interface of the critical nucleus with  $R_{1,c}$  and  $R_{2,c}$  being the principal radii of curvature of the surface (the surface is oriented with the unit normals pointing toward the liquid). For brevity, we will refer to  $k_c$  simply as “curvature” in the remainder of this paper.  $A^{\text{LV}}$  and  $A^{\text{SV}}$  are the areas of the liquid–vapor and solid–vapor interfaces, respectively. The reference state is chosen to be the metastable liquid state in the absence of a vapor nucleus [as depicted in Fig. 1(a)], and the following conditions for equilibrium have been incorporated:

- (i) Uniformity of temperature across all phases,

$$T^{\text{R}} = T^j = T^{jk}, \quad (3)$$

where  $j = \text{L or V}$ , and  $jk = \text{LV, SL, or SV}$  representing bulk phases and interfaces, respectively.

- (ii) Equality of chemical potentials of each component in each subsystem,

$$\mu_i^j = \mu_i^k = \mu_i^{jk}, \quad (4)$$

where the subscript denotes the component  $i$ . In this work, we use  $i = 1$  for the solvent and  $i = 2$  for the gas.

- (iii) Mechanical equilibrium conditions,

$$\sigma^{\text{SV}} = \sigma^{\text{SL}} + \sigma^{\text{LV}} \cos \theta_{\text{eq}}, \quad (5)$$

$$P^{\text{L}} = P^{\text{R}}, \quad (6)$$

$$P^{\text{V}} - P^{\text{L}} = \sigma^{\text{LV}} k_c. \quad (7)$$

$\sigma^{\text{SV}}$  and  $\sigma^{\text{SL}}$  in Eq. (5) are the interfacial tensions of the solid–vapor and solid–liquid interfaces, respectively.

For the derivation of Eq. (2), it is also assumed that the liquid surrounding the critical nucleus is large enough that the temperature and pressure changes due to the formation of the nucleus can be neglected. Additionally, since the number of molecules of various components that go into the creation of the critical nucleus

can be shown to be small compared to the number of molecules in the solution, the concentration of the components in the solution can be assumed to be constant. Consequently, the variations in the chemical potentials of components in the solution can also be neglected because they are functions of temperature, pressure, and concentration only.<sup>39</sup>

### III. NONIDEAL MULTICOMPONENT LIQUID–VAPOR EQUILIBRIUM ACROSS A CURVED INTERFACE

For heterogeneous nucleation of a vapor bubble from a pure liquid, the critical curvature,  $k_c$ , in Eq. (2) can be found by knowing the vapor pressure of the liquid at the given temperature and using a version of the Kelvin equation<sup>51</sup> generalized to nonspherical liquid–vapor interfaces. In the presence of other components, however, the equations for multicomponent liquid–vapor equilibrium need to be established first while considering the geometry (i.e., the curvature of the liquid–vapor interface). Since the pressure is not uniform in the system, the applicability of the typical phase equilibrium equations for uniform pressure (i.e.,  $P = P^{\text{L}} = P^{\text{V}}$ ) from the literature needs to be checked, and the necessary modifications should be made. Here, we give a detailed derivation of the liquid–vapor equilibrium equations for the general case where  $P^{\text{L}} \neq P^{\text{V}}$ . We start by writing the equality of chemical potentials [Eq. (4)] in liquid and vapor phases for both components,

$$\mu_1^{\text{L}}(T, P^{\text{L}}, x_1) = \mu_1^{\text{V}}(T, P^{\text{V}}, y_1), \quad (8)$$

$$\mu_2^{\text{L}}(T, P^{\text{L}}, x_2) = \mu_2^{\text{V}}(T, P^{\text{V}}, y_2), \quad (9)$$

where  $x_i$  and  $y_i$  are the mole fractions of the components in the liquid and vapor phases, respectively. Considering the pressures in the systems of interest can be quite high, we do not make ideal-gas assumptions *a priori*. For the solvent, using the definition of fugacity,<sup>53</sup> Eq. (8) can be rewritten as

$$\mu_1^{\text{L}}(T, P^{\text{L}}, x_1 = 1) + \bar{R}T \ln \left( \frac{\hat{f}_1^{\text{L}}}{f_1^{\text{L}}} \right) = \mu_1^{\text{V}}(T, P^{\text{V}}, y_1 = 1) + \bar{R}T \ln \left( \frac{\hat{f}_1^{\text{V}}}{f_1^{\text{V}}} \right), \quad (10)$$

where  $f_i^{\text{L}}$  is the fugacity of pure component  $i$  as a liquid at  $T$  and  $P^{\text{L}}$ ,  $\hat{f}_i^{\text{L}}$  is the fugacity of component  $i$  in a liquid mixture (i.e., in the presence of other components) at  $T$  and  $P^{\text{L}}$ ,  $f_i^{\text{V}}$  is the fugacity of pure component  $i$  as a vapor at  $T$  and  $P^{\text{V}}$ ,  $\hat{f}_i^{\text{V}}$  is the fugacity of component  $i$  in a vapor mixture at  $T$  and  $P^{\text{V}}$ , and  $\bar{R}$  is the universal gas constant. In the framework of our problem, the solvent component is always kept subcritical. Hence, for convenience, the state at which the pressure is equal to the saturation pressure of the solvent,  $P_{1,\text{sat}}$ , at temperature  $T$ , can be chosen as the reference state. Using the Gibbs–Duhem equation, we can write<sup>54</sup>

$$\begin{aligned} \mu_1^{\text{L}}(T, P_{1,\text{sat}}, x_1 = 1) + \int_{P_{1,\text{sat}}}^{P^{\text{L}}} v_1^{\text{L}} dP + \bar{R}T \ln \left( \frac{\hat{f}_1^{\text{L}}}{f_1^{\text{L}}} \right) \\ = \mu_1^{\text{V}}(T, P_{1,\text{sat}}, y_1 = 1) + \bar{R}T \ln \left( \frac{\hat{f}_1^{\text{V}}}{f_1^{\text{V}}} \right), \end{aligned} \quad (11)$$

where  $v_1^L$  is the molar volume of pure liquid solvent. For a component  $i$  in a liquid solution, the activity coefficient is defined as  $\gamma_i \equiv \hat{f}_i^L/x_i f_i^L$ , and the fugacity coefficient is defined as  $\hat{\phi}_i^V \equiv \hat{f}_i^V/y_i P^V$ .<sup>53</sup> Note that the pure component activity coefficient is unity [i.e.,  $\lim_{x_i \rightarrow 1} (\gamma_i) = 1$ ]. However, note that the pure gas fugacity coefficient is not necessarily unity:  $\hat{\phi}_i^V = \lim_{y_i \rightarrow 1} (\hat{\phi}_i^V) = f_i^V/P^V$ . Using these definitions and the equality of chemical potentials of the liquid and vapor of pure solvent at saturation, we can write

$$\hat{\phi}_1^V \gamma_1 P^V = x_1 \gamma_1 \phi_{1,\text{sat}} P_{1,\text{sat}} \eta_1, \quad (12)$$

where  $\phi_{1,\text{sat}}$  is the fugacity coefficient of the vapor of pure solvent at saturation, and  $\eta_1$  is defined as

$$\eta_1 \equiv \exp\left(\frac{\int_{P_{1,\text{sat}}}^{P^L} v_1^L dP}{RT}\right). \quad (13)$$

Equation (12) is a practically more useful version of Eq. (8) for the equality of the chemical potential of the solvent between the phases.

Since the typical gas component is usually supercritical at the conditions of interest (e.g., nitrogen or carbon dioxide at 50 °C),  $P_{2,\text{sat}}$  may not be defined at  $T$ , and the pure gas component at saturation cannot be chosen as the reference state. Instead, we first consider a state where both vapor and solution are at the pressure  $P^L$  with arbitrary concentrations of gas as  $x_2'$  and  $y_2'$  in the solution and in the vapor phases, respectively. Using Eq. (9), we write

$$\mu_2^L(T, P^L, x_2') + \bar{R}T \ln\left(\frac{\hat{f}_2^L}{\hat{f}_2^L(P^L)}\right) = \mu_2^V(T, P^L, y_2') + \bar{R}T \ln\left(\frac{\hat{f}_2^V}{\hat{f}_2^V(P^L)}\right). \quad (14)$$

For clarity, in the parentheses, we indicate the pressure at which the quantity needs to be evaluated if it is different than what is indicated by the phase descriptor (i.e., the superscript letter). Using the definitions of the fugacity and activity coefficients and rearranging, Eq. (14) can be rewritten as

$$\mu_2^V(T, P^L, y_2') - \mu_2^L(T, P^L, x_2') = \bar{R}T \ln\left(\frac{x_2 \gamma_2 \hat{\phi}_2^V(P^L) y_2' P^L}{x_2' \gamma_2' \hat{\phi}_2^V y_2' P^V}\right). \quad (15)$$

Now, we choose  $P_{1,\text{sat}}$  as the reference pressure for the left-hand side of Eq. (15) and write

$$\begin{aligned} \mu_2^V(T, P_{1,\text{sat}}, y_2') - \mu_2^L(T, P_{1,\text{sat}}, x_2') + \bar{R}T \ln\left(\frac{\hat{f}_2^V(P^L)}{\hat{f}_2^V(P_{1,\text{sat}})}\right) \\ - \int_{P_{1,\text{sat}}}^{P^L} \bar{v}_2^L dP = \bar{R}T \ln\left(\frac{x_2 \gamma_2 \hat{\phi}_2^V(P^L) y_2' P^L}{x_2' \gamma_2' \hat{\phi}_2^V y_2' P^V}\right), \end{aligned} \quad (16)$$

where  $\bar{v}_2^L$  is the partial molar volume of the gas component in the solution at  $x_2'$ . By rearranging and taking the limit as  $x_2' \rightarrow 0$  of both sides of Eq. (16), we can write

$$\begin{aligned} \lim_{x_2' \rightarrow 0} [\mu_2^V(T, P_{1,\text{sat}}, y_2') - \mu_2^L(T, P_{1,\text{sat}}, x_2')] \\ = \lim_{x_2' \rightarrow 0} \left[ \bar{R}T \ln\left(\frac{x_2 \gamma_2 \hat{\phi}_2^V(P_{1,\text{sat}}) y_2' P_{1,\text{sat}}}{x_2' \gamma_2' \hat{\phi}_2^V y_2' P^V}\right) + \int_{P_{1,\text{sat}}}^{P^L} \bar{v}_2^L dP \right]. \end{aligned} \quad (17)$$

Instead of keeping  $y_2'$  independent, for a small  $x_2'$  chosen arbitrarily close to zero, we choose an equilibrium concentration  $y_2'$  (also close to zero) such that the vapor pressure is equal to  $P_{1,\text{sat}}$  (the vapor is almost entirely component 1), which makes the left-hand side of Eq. (17) vanish. Additionally, one can make the following definitions at this equilibrium:

- (i) Infinite dilution activity coefficient of component 2,

$$\gamma_2^* \equiv \lim_{x_2' \rightarrow 0} \left(\frac{y_2'}{x_2'}\right). \quad (18)$$

Note that  $\lim_{x_2' \rightarrow 0} (\gamma_2^*) = 1$  (i.e.,  $\gamma_2^*$  is normalized to unity at  $x_2 \rightarrow 0$ ).

- (ii) Partial molar volume of component 2 in solution at infinite dilution,

$$\bar{v}_{2,\infty}^L \equiv \lim_{x_2' \rightarrow 0} (\bar{v}_2^L). \quad (19)$$

- (iii) The ratio of fugacity in the vapor to the concentration in the liquid of component 2 at infinite dilution,

$$H_{12} \equiv \lim_{x_2' \rightarrow 0} \left[ \frac{\hat{\phi}_2^V(P_{1,\text{sat}}) y_2' P_{1,\text{sat}}}{x_2'} \right], \quad (20)$$

which is the Henry's law constant by definition.<sup>55,56</sup>

Substituting these definitions into Eq. (17) and rearranging, the liquid–vapor equilibrium for the gas component across a curved interface can be expressed as

$$\hat{\phi}_2^V y_2 P^V = x_2 \gamma_2^* H_{12} \eta_2, \quad (21)$$

where  $\eta_2$  is defined as

$$\eta_2 \equiv \exp\left(\frac{\int_{P_{1,\text{sat}}}^{P^L} \bar{v}_{2,\infty}^L dP}{RT}\right). \quad (22)$$

Like Eq. (12), Eq. (21) is a practically more useful version of Eq. (9). Equations (12) and (21) together establish the nonideal liquid–vapor equilibrium for a liquid–gas mixture, which, in general, may have different phase pressures. Note that by setting  $P = P^V = P^L$  in Eqs. (12) and (21), we recover the two-component liquid–vapor equilibrium equations across a flat interface.<sup>53</sup>

By combining Eqs. (12) and (21) with Eq. (7) and noting that  $P^V = y_1 P^V + y_2 P^V$ , we can write

$$k_c = \left( \frac{x_1 \gamma_1 \phi_{1,\text{sat}} P_{1,\text{sat}} \eta_1}{\hat{\phi}_1^V} + \frac{x_2 \gamma_2^* H_{12} \eta_2}{\hat{\phi}_2^V} - P^L \right) / \sigma^{LV}. \quad (23)$$

Equation (23) relates the equilibrium thermodynamic properties of the mixture to the equilibrium geometry. It can be viewed (after some rearranging) as the nonideal Kelvin equation for a liquid–gas mixture, generalized to an arbitrary constant-mean-curvature interface shape.

When dealing with aqueous systems, it is customary to use an activity model for the liquid phase activity coefficients,  $\gamma_1$  and  $\gamma_2^*$ , and an equation of state for the vapor phase fugacity coefficients,

$\phi_1^V$  and  $\phi_2^V$ , to correlate them to other variables and/or known parameters (the so-called  $\gamma$ - $\phi$  approach/model). This method generally produces a more accurate description compared to, for example, using the same equation of state for both liquid and vapor while still being relatively simple. We use the nonrandom two-liquid model<sup>57</sup> for the activity in solution and the Peng–Robinson cubic equation of state<sup>58</sup> for the vapor phase fugacity. Since the only solvent in this work is water, the parameters  $\phi_{1,\text{sat}}$ ,  $P_{1,\text{sat}}$ ,  $v_1^L$ ,  $H_{12}$ , and  $\bar{v}_{2,\infty}^L$  in Eqs. (12) and (21) can be accurately obtained from the tabulated values and/or functional correlations from the literature. For nitrogen–water and carbon dioxide–water solutions, the model we have chosen provides enough accuracy for pressures up to 100 MPa at moderate temperatures (see Figs. S2 and S3). This pressure range is sufficient to describe equilibrium across a spherical liquid–vapor interface with a radius of curvature down to  $\sim 1.4$  nm, assuming negligible pressure at the low-pressure side (for  $\sigma^{\text{LV}} = 0.068$  J/m<sup>2</sup>—the value at  $T = 323.15$  K). For comparison, a critical nucleus (having a free energy barrier of  $\sim 35k_B T$ ; see Sec. IV) for heterogeneous vapor nucleation from liquid water on a hydrophobic flat substrate with a contact angle of  $120^\circ$  (i.e., a spherical cap) has a radius of curvature of  $\sim 2$  nm. This presents the worst-case scenario because the critical nuclei corresponding to the same energy barrier in nanoconfinement need not be as curved (mean curvature implied). Note that the liquid-phase pressure is allowed to be negative (i.e., tension), although there are no experimental data available for this case since most experiments are performed at the macroscopic scale with a flat liquid–vapor interface (i.e., uniform pressure; negative pressure is not defined for a gas). A detailed description of the thermodynamic model, the correlations used, and the validation against available experimental data are given in the supplementary material.

#### IV. ESTIMATING FREE ENERGY BARRIER FROM EXPERIMENTS

We use classical nucleation theory to estimate the free energy barrier from the nucleation rate, which has been applied to nanopores before in Refs. 15 and 36. To summarize, the probability of fluctuations in the thermodynamic properties of liquids is inversely proportional to the exponential of the reversible work associated with such fluctuations. For the formation of a vapor bubble, this reversible work is the corresponding free energy barrier. Written in units of expected nucleation events per unit length of the pore,  $l_p$ , per unit time, the nucleation rate is given as<sup>36</sup>

$$J = \frac{Z\nu}{b} \exp\left(-\frac{\Delta B_c}{k_B T}\right), \quad (24)$$

where  $Z$  is the barrier transmission coefficient (also known as the Zeldovich factor),  $b$  and  $\nu$  are the microscopic length and frequency scales, respectively, and  $\Delta B_c$  denotes the free energy barrier. Note that Refs. 15 and 36 use the transition state theory approximation to extract the nucleation energy barriers, which presumes negligible barrier recrossings (i.e.,  $Z = 1$ ). This approximation is questionable because of the flat energy profiles and diffusive propagation characteristics of nucleation.<sup>59</sup> Indeed, for capillary drying of water in a hydrocarbon-like slit, the transmission coefficient was found to be  $Z \sim 0.01$ – $0.1$ .<sup>23</sup>

Since  $J$  depends much more strongly on  $\Delta B_c$  than the pre-exponential factor, the dependence of  $\nu$  on pore radius is neglected. The typical values of  $b$  and  $\nu$  for pure water are  $\sim 0.1$ – $1$  nm and  $\sim 10^{12}$ – $10^{13}$  Hz, respectively.<sup>15,36</sup> We will assume that these values are also applicable to the liquid–gas solutions considered in this work.

To estimate the free energy barrier that is low enough for the nucleation event to be observable in typical experimental time,  $t$ , one usually sets  $Jtl_p = 1$ . Using this value, we can invert Eq. (24) to find the energy barrier,

$$\Delta B_c = k_B T \ln\left(\frac{Zt\nu l_p}{b}\right). \quad (25)$$

Typical cylindrical nanopores have lengths of hundreds of nanometers ( $l_p \sim 100$ – $1000$  nm),<sup>60–62</sup> and typical experimental times range from a fraction of a second to a few tens of seconds ( $t \sim 0.1$ – $100$  s). By substituting the parameters from the listed ranges above in Eq. (25), one calculates  $\Delta B_c \sim 25k_B T$  as the lowest value, and  $\Delta B_c \sim 44k_B T$  as the highest value, with the average being  $\Delta B_c = 35k_B T$ . We use this average as a representative value of the energy barrier, where applicable, in the following sections. Since the energy barrier scales with the square of the pore radius, this translates to  $\sim 12\%$  uncertainty for the inference of the pore size. Note that about  $2/3$  of the uncertainty in  $\Delta B_c$  is eliminated with information about the pore length in the experiment and the observation time. For example, for the drying of an average-sized pore of length 500 nm that is observed for 10 seconds, the range becomes  $\Delta B_c \sim 32$ – $38k_B T$ .

#### V. SHAPE OF THE CRITICAL NUCLEUS

Once the chemical equilibrium is solved at given conditions, the critical curvature of the liquid–vapor interface,  $k_c$ , is known from Eq. (23) (see the supplementary material for the details of the solution procedure). Next, the goal is to find a nucleus shape inside a cylinder whose liquid–vapor interface has the curvature  $k_c$  and calculate the free energy barrier corresponding to this shape. If there are more than one nucleus geometry corresponding to  $k_c$ , the one with the lowest free energy should be chosen as the critical nucleus. Following Ref. 36, two distinct possibilities are considered for the shape of the critical nucleus confined to a cylinder wall: (i) an annulus shape—a symmetric nucleus with the axis of symmetry being the cylinder axis and with two disjoint three-phase contact lines [Fig. 1(e)], and (ii) a saddle shape—a localized nucleus on the wall of the cylinder with one continuous three-phase contact line [Fig. 1(d)]. To our knowledge, only the symmetric nucleus has a known analytical solution, details of which can be found in Ref. 36 (see the supplementary material for the main equation written in our notation). To determine the geometry of the localized nucleus, we use Surface Evolver,<sup>63</sup> which is a specialized software package designed for complex variational problems involving surface forces.

Briefly, the Surface Evolver code tries to minimize the energy of a surface subject to constraints, such as fixed volume of the nucleus and fixed walls with surface energy. The surface of the shape to be evolved is approximated by triangles (i.e., the surface is represented as a simplicial complex) that are moved toward an equilibrium (minimum-energy) shape by gradient descent or conjugate gradient

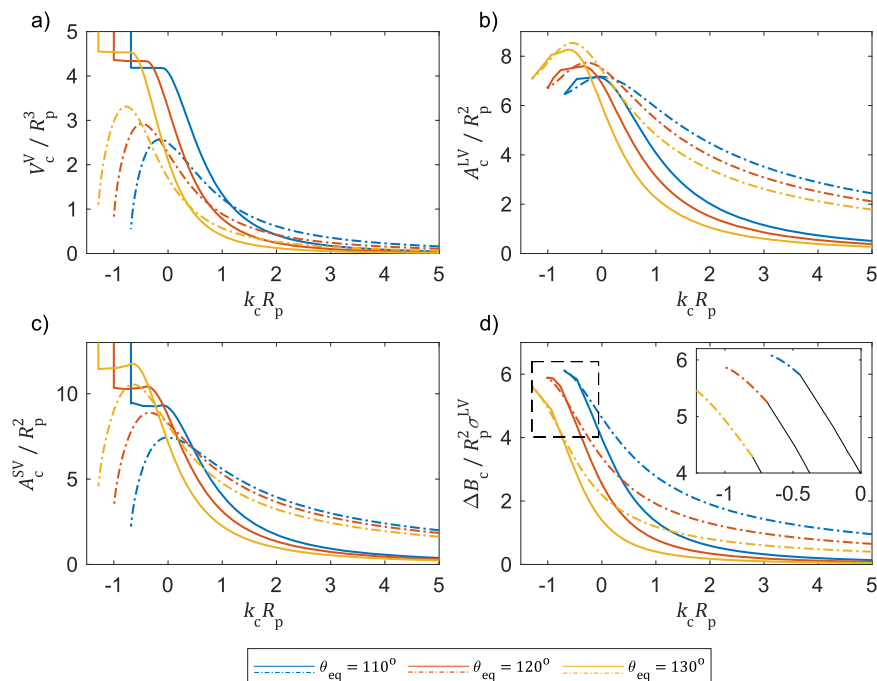


**FIG. 2.** Nondimensional geometrical quantities for the critical nuclei and the corresponding energy plots as functions of nondimensional curvature for three different contact angles: blue for  $\theta_{\text{eq}} = 110^\circ$ , orange for  $\theta_{\text{eq}} = 120^\circ$ , and yellow for  $\theta_{\text{eq}} = 130^\circ$ . The solid lines are for the localized nuclei, and the dotted-dashed lines are for the symmetric nuclei. Panels (a)–(c) show the plots of volume, liquid–vapor interfacial area, and solid–vapor interfacial area, respectively. Panel (d) shows the plots of the energy barrier as calculated using Eq. (2). The inset shows a zoom-in of the curvature range where the symmetric nuclei have slightly lower energy. Here, the energy curves for the localized nuclei are shown in black to highlight the transition points.

methods. The shape usually converges very fast, although the accuracy may depend on the mesh size as well as the number of evolution steps. Surface Evolver works in a unitless system (i.e., it only deals with numerical values) in that the user is free to assign a consistent system of units of measurement to relate the results to real-world applications. The volume of the shape is calculated by evaluating surface integrals (Gauss's theorem), and the solid–vapor interfacial area is calculated by evaluating a line integral over the contact line (Stokes's theorem). This eliminates the need to cover the solid surfaces with otherwise useless facets. More details about Surface Evolver can be found elsewhere.<sup>63</sup>

In general, it is not practical to run Surface Evolver with a prescribed curvature because stability becomes an issue. Instead, we created a series of saddle-shaped nuclei in the volume range from 0.1 to 7 (with an increment of 0.05; a total of 139 points) for contact angles  $110^\circ$ ,  $120^\circ$ , and  $130^\circ$  in a unit cylinder (radius of 1) and generated look-up tables for the curvature and the area of the liquid–vapor interface, the area of the solid–vapor interface, and the length of the three-phase contact line. This way, after converting the tabulated values to a consistent system of units for a given pore radius, the quantities can be interpolated in the table for the prescribed critical curvature. The free energy barrier can be calculated using these values directly in Eq. (2). Then, the volume and the areas can be varied following the trends around this equilibrium to investigate the stability of the equilibrium.

The summary of nondimensionalized results of geometry calculations is given in Fig. 2, panels (a)–(c) for both symmetric (dotted–dashed lines) and localized nuclei (solid lines) and for three different values of contact angle. The quantities are plotted against the dimensionless critical curvature,  $k_c R_p$ . The corresponding free energy barriers are given in panel (d) as calculated using Eq. (2). It

is seen that the symmetric nucleus is only slightly preferred when the prescribed curvature is close to the minimum possible curvature in the pore (i.e.,  $k_c R_p \sim 2 \cos \theta_{\text{eq}}$ ). This is in complete agreement with previous results.<sup>15,36</sup> Note that there are infinite solutions for the shape of the nucleus when  $k_c R_p = 2 \cos \theta_{\text{eq}}$  with different volumes and solid–vapor interfacial areas, which all have the same liquid–vapor interfacial areas and energies. These correspond to the vapor nuclei sealed with two disjoint spherical caps at both ends. The end points of the curves in panels (b) and (d) indicate the transition to the two-disjoint-spherical-caps geometry. For  $k_c R_p < 2 \cos \theta_{\text{eq}}$ , there are no solutions, meaning that the pore cannot dry at such conditions.

Examples of the lowest energy shapes for the prescribed curvature are given in Fig. 3 for contact angle  $\theta_{\text{eq}} = 120^\circ$ . These examples are chosen from ranges where they have lower energy compared to the other geometry. The curvatures of the localized nuclei in panels (a) and (b) are  $k_c R_p = 0.83$  and  $k_c R_p = 0.21$ , respectively. In panel (c), the two-dimensional slices of three symmetric nuclei with curvatures  $k_c R_p = -0.8$  (dotted line),  $-0.87$  (dashed line), and  $-0.94$  (solid line) are shown. For the equation used to calculate these profiles, see the supplementary material.

It is important to discuss the reasonableness of both nucleus geometries in the context of the physical theory, which has not been addressed in the previous studies. One of the main assumptions of classical nucleation theory is that the primary dynamic variable of interest (i.e., the reaction coordinate) is the number of molecules in the nucleus and that other variables equilibrate much faster.<sup>48,64</sup> The number of molecules is often well approximated by the volume of the nucleus. From atomistic simulations in nanopores, it has been concluded that, even for a pore with a radius  $R_p \sim 1$  nm, the volume of the nucleus alone is a good choice for the reaction coordinate.<sup>23</sup>

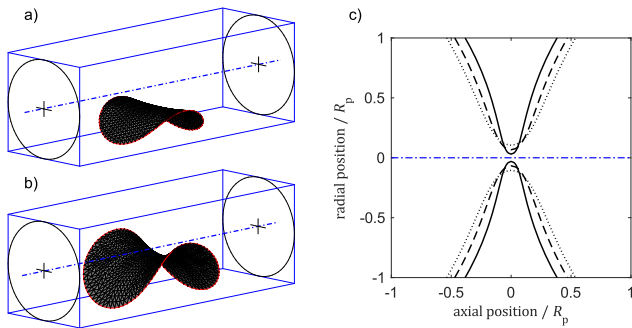


**FIG. 3.** Examples of the localized (a) and (b) and symmetric (c) nuclei. As calculated using Surface Evolver, the three-dimensional views of the liquid–vapor interfaces for the localized nuclei are shown in panels (a) and (b), which have constant curvatures of  $k_c R_p = 0.83$  and  $k_c R_p = 0.21$ , respectively. For clear views of these shapes, only the contours of the cylinders are shown at the ends of the bounding boxes. The three-phase contact lines are shown in red. In panel (c), the two-dimensional views of three symmetric nuclei on an axial plane are shown. The three-dimensional surfaces are obtained by rotating these profiles around the cylinder axis (blue, dotted–dashed line). These surfaces have constant curvatures of  $k_c R_p = -0.8$  (dotted line),  $-0.87$  (dashed line), and  $-0.94$  (solid line).

This means that the shape found by solving the variational problem for a prescribed curvature should also be the minimum energy shape at that volume to describe a critical nucleus. To test this, the symmetry constraint should be removed since there is no physical basis for this requirement. In other words, a symmetric nucleus should be allowed to transform into a localized nucleus if this transition is energy-minimizing. For a given volume in the volume range where symmetric nuclei are possible [see Fig. 2(a)], there are two or three solutions, one of which is the localized nucleus. Using their corresponding curvatures on the energy plot [Fig. 2(d)], we see that the localized nucleus always has the lowest energy for a given volume up to the maximum volume above which only the disjoint-spherical-caps geometry is possible. We confirmed this using Surface Evolver by initializing the shapes symmetrically for prescribed volumes, which, upon evolution toward minimum energy, quickly destabilized and transformed into localized nuclei. Therefore, we believe that the formation of the symmetric nuclei (excluding the disjoint-caps geometry) as part of the nucleation path is unlikely in a physical system. In the remainder of this paper, we only consider either the localized geometry or the two-spherical-caps geometry (at large volumes when a localized nucleus is not possible) as the shape of the critical nucleus. However, it is worth noting that the nucleation barrier is only slightly different in a small range of curvature values [see the inset in Fig. 2(d)] depending on the choice of symmetric or localized geometry as the critical nucleus shape in the potential range. Therefore, both our qualitative and quantitative results would not be altered noticeably, even if symmetric nuclei were physically possible.

As part of the discussion of the nucleus shape, it is instructive to highlight the importance of the confinement geometry and its effect on the phase transition. It is due to the shape of the confinement that the nuclei with close to zero and negative (according to our sign convention) curvatures are also energy-minimizing. For pores small enough so that the corresponding free energy barrier is  $\Delta B_c \sim 35k_B T$ , this means that, even at conditions where  $P^L \gg P^V$ ,

the liquid-to-vapor transition can happen. Without the confinement geometry of the pore,  $P^L \ll P^V$  is required for phase transition because the energy-minimizing nuclei would necessarily have spherical liquid–vapor interfaces with  $k_c > 0$  while also having to be small to satisfy  $\Delta B_c \sim 35k_B T$ .

## VI. RESULTS

### A. Comparison of free energy profiles

Next, we investigate the effects of dissolved nitrogen and carbon dioxide in water on the nucleation free energy barrier. Here, it is convenient to introduce an auxiliary variable,  $S$ , termed the saturation ratio, defined as the ratio of the concentration of the gas in the liquid phase to the saturation concentration at the intrusion pressure:  $S = x_2/x_{2,\text{sat}}@P_{\text{int}}$ . We consider three pore sizes:  $R_p = 1, 1.5,$  and  $2$  nm, and three contact angles:  $\theta_{\text{eq}} = 110^\circ, 120^\circ,$  and  $130^\circ$  since these are the typical sizes of the pores and the typical contact angles of the materials used in the experiments. The advancing contact angle,  $\theta_a$ , used to calculate the intrusion pressure is taken to be equal to the equilibrium contact angle,  $\theta_{\text{eq}}$ . This choice does not affect the results because a slight incorrect estimation of the intrusion pressure, which is only needed to estimate the gas concentration, is compensated by varying the gas concentration independently around this saturation value. The temperature is fixed at  $T = 323.15$  K (to avoid subcriticality and potential error in the phase description of carbon dioxide below its critical temperature of  $304.13$  K). The interfacial tension of liquid with vapor is taken to be constant and equal to the surface tension of pure water at  $T = 323.15$  K ( $\sigma^{LV} = 0.068$  J/m<sup>2</sup>). Studies on the effects of dissolved gas have shown that the water surface tension is lower when the gas is present (as low as  $\sigma^{LV} = 0.030$  J/m<sup>2</sup> for dissolved carbon dioxide at high pressures).<sup>65,66</sup> The adsorption of the gas at the solid–liquid interface would also decrease the solid–liquid interfacial tension with both changes in  $\sigma^{SL}$  and  $\sigma^{LV}$  affecting the contact angle. Assuming these effects are comparable in size, the inclusion of only one of them is expected to give worse predictions compared to if both effects are neglected. Quantifying these effects is beyond the scope of this paper, and with only the former effect being well-documented in the literature<sup>65,66</sup> (and not at the nanoscale), we will assume that, in the presence of the gas, the interfacial tension of the liquid–vapor interface and the contact angle are equal to those of pure water.

Assuming a localized nucleus, the free energy plots [calculated using Eq. (2)] are given in Fig. 4 for  $\theta_{\text{eq}} = 110^\circ$ , in Fig. 5 for  $\theta_{\text{eq}} = 120^\circ$ , and in Fig. 6 for  $\theta_{\text{eq}} = 130^\circ$ . Only the region up to the transition to the two-disjoint-spherical-caps geometry is shown. The intrusion pressures are calculated using Eq. (1) for each pore size and contact angle combination. In these three figures, each row of plots is for a different pore size, and the columns are for different liquid pressures. For each plot, the  $x$  axis is the volume of the nucleus in nm<sup>3</sup>, and the  $y$  axis is the energy in units of  $k_B T$ . The  $\Delta B = 35k_B T$  limit is shown by the horizontal solid black line on each subplot for visual reference. The green lines correspond to the pure-water case, while the orange lines are for nitrogen dissolved in water, and the light blue lines are for carbon dioxide dissolved in water. The lines are solid for  $S = 1$ , dashed for  $S = 2$ , and dotted–dashed for  $S = 0.5$ . All curves are highlighted in red around the critical volume and the corresponding free energy barrier, indicating an unstable

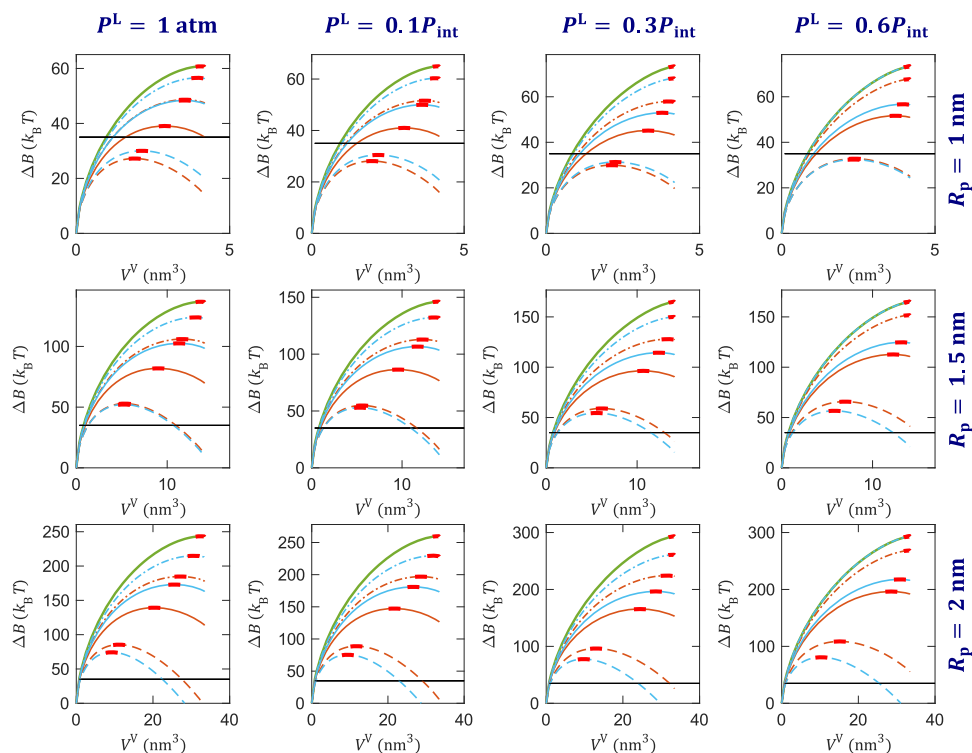


**FIG. 4.** Free energy plots for  $\theta_{\text{eq}} = 110^\circ$  at different pore radii, liquid pressures, and saturation ratios. The temperature is fixed at  $T = 323.15$  K. The green lines are for pure water, the light blue lines are for water with dissolved carbon dioxide, and the orange lines are for water with dissolved nitrogen. Each row of subplots is for a different pore radius, while the columns are for different liquid pressures. The solid lines are for  $S = 1$ , the dashed lines are for  $S = 2$ , and the dotted-dashed lines are for  $S = 0.5$ . The horizontal solid black lines represent  $\Delta B = 35k_B T$  for visual reference. All curves are highlighted in red around the critical volume and the corresponding free energy barrier.

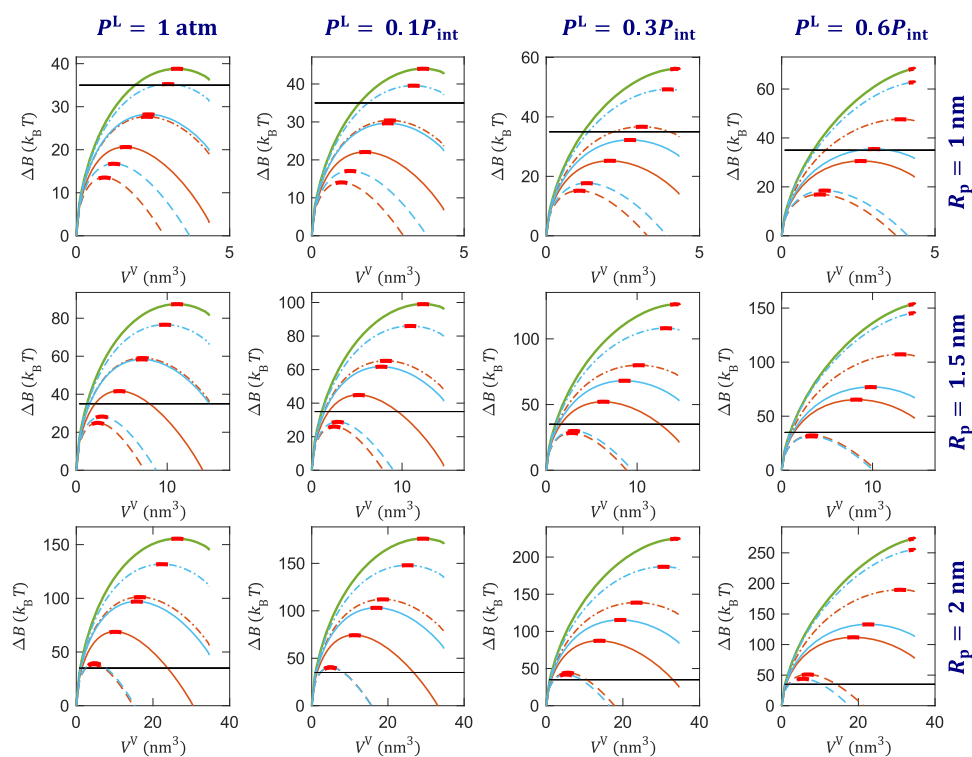


**FIG. 5.** Free energy plots for  $\theta_{\text{eq}} = 120^\circ$  at different pore radii, liquid pressures, and saturation ratios. The temperature is fixed at  $T = 323.15$  K. The green lines are for pure water, the light blue lines are for water with dissolved carbon dioxide, and the orange lines are for water with dissolved nitrogen. Each row of subplots is for a different pore radius, while the columns are for different liquid pressures. The solid lines are for  $S = 1$ , the dashed lines are for  $S = 2$ , and the dotted-dashed lines are for  $S = 0.5$ . The horizontal solid black lines represent  $\Delta B = 35k_B T$  for visual reference. All curves are highlighted in red around the critical volume and the corresponding free energy barrier.

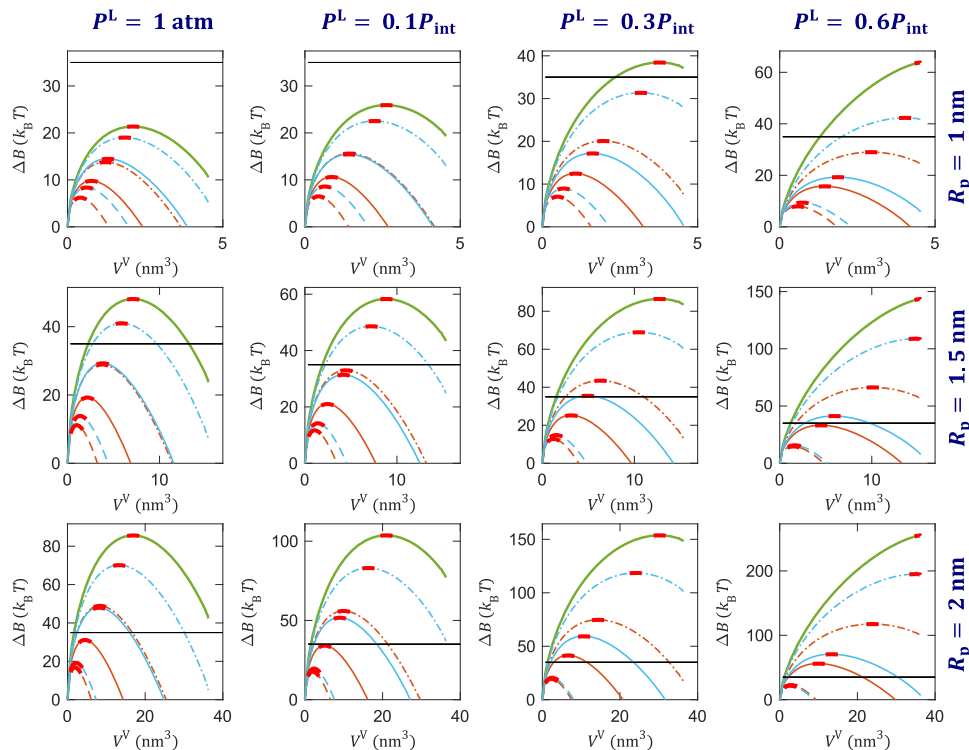


**FIG. 6.** Free energy plots for  $\theta_{\text{eq}} = 130^\circ$  at different pore radii, liquid pressures, and saturation ratios. The temperature is fixed at  $T = 323.15$  K. The green lines are for pure water, the light blue lines are for water with dissolved carbon dioxide, and the orange lines are for water with dissolved nitrogen. Each row of subplots is for a different pore radius, while the columns are for different liquid pressures. The solid lines are for  $S = 1$ , the dashed lines are for  $S = 2$ , and the dotted-dashed lines are for  $S = 0.5$ . The horizontal solid black lines represent  $\Delta B = 35k_B T$  for visual reference. All curves are highlighted in red around the critical volume and the corresponding free energy barrier.

equilibrium in all cases. Overall, the presence of the gas is seen to decrease the free energy barrier significantly in most cases; the higher the gas concentration, the easier it is to nucleate. This is because of increased vapor pressure due to the presence of the gas.

### B. Importance of mixture nonideality

In the literature,<sup>19,25,27</sup> the effects of gas on nucleation are often quantified by assuming simple, ideal solution theories such as Henry's or Raoult's laws. For gases that have very low solubility, the error because of this assumption is not expected to be large. By taking  $\gamma_1 = \gamma_2^* = \hat{\phi}_2 = \hat{\phi}_1 = \phi_{1,\text{sat}} = \eta_1 = \eta_2 = 1$ , Eq. (21) reduces to Henry's law and Eq. (12) to Raoult's law. Here, the model with these assumptions is referred to as the ideal model. Note that, for nitrogen in water, we already assume  $\gamma_1 = \gamma_2^* = 1$ , even for the nonideal model (see the supplementary material). We compare the primary parameter of interest in this study—the free energy barrier—of both nonideal and ideal models in Fig. 7. The orange lines are for the nonideal nitrogen–water system, the light blue lines are for the nonideal carbon dioxide–water system, and the purple dashed lines are for the ideal model. Notice that, for the ideal model, the type of gas is irrelevant because the vapor pressure does not depend on the liquid pressure. We consider three pore sizes (the same pore sizes as above), and the concentration of gas in the liquid is set to be the saturation concentration at the pore intrusion pressure. Since the carbon dioxide–water system exhibits a highly nonideal behavior at the pressures of interest (see Fig. S3), we see large deviations between the predictions of the two models. The nonideal and ideal curves for the nitrogen–water system follow the same trend while still being

noticeably different. For instance, in a 1.5 nm radius pore, the ideal model overestimates the drying pressure for the carbon dioxide–water mixture by  $\sim 40$  MPa and for the nitrogen–water mixture by  $\sim 20$  MPa [using  $\Delta B_c = 35k_B T$ ; Fig. 7(b)]. On all panels of Fig. 7, the intersection points of the three free energy barrier curves correspond to the intrusion pressure of the pore. Consequently, the critical nucleus at this point has a liquid–vapor interface with zero (mean) curvature.

### C. Extrusion pressures and effect of line tension

Previous studies<sup>15,36,67</sup> have found that the free energy barrier calculated from Eq. (2) for pure water (see green curves on Figs. 4–6) is too high to match the experiments. Additionally, atomistic simulations in collective variables<sup>67</sup> have shown that, even though the saddle-shaped nucleus is a good approximation, the energy barrier is significantly lower than what is predicted by Eq. (2). In both cases, it was possible to match the predictions of Eq. (2) (using the geometry from Surface Evolver) and the results from the experiments or simulations by adding an energy term to Eq. (2) proportional to the length of the three-phase contact line. While these may seem like attempts to artificially force classical nucleation theory to agree with the observations, it is often found that a quantitative equivalence can be established for the complex physics due to the small size by assigning energy to the three-phase contact line (the so-called apparent or effective line tension).<sup>68–74</sup> For instance, excellent agreement could be achieved between the heterogeneous nucleation experiments and the predictions of classical nucleation theory by including a line tension term in the free energy equation.<sup>75</sup>

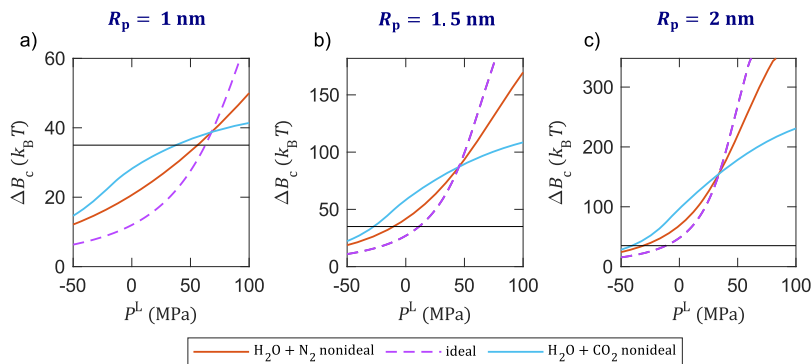


**FIG. 7.** Comparison of free energy barriers as functions of liquid pressure for ideal and nonideal solution models for three different pore sizes: (a)  $R_p = 1$  nm, (b)  $R_p = 1.5$  nm, and (c)  $R_p = 2$  nm. The orange lines are for nitrogen–water, and the light blue lines are for carbon dioxide–water. The solid lines correspond to the nonideal model, while the dashed lines correspond to the ideal model. The concentration of the gas in the solution is the saturation value at the intrusion pressure of each pore. The horizontal solid black lines represent  $\Delta B = 35k_B T$  for visual reference. All calculations were performed for  $\theta_a = \theta_{eq} = 120^\circ$ ,  $T = 323.15$  K, and  $\sigma^{LV} = 0.068$  J/m<sup>2</sup>.

Additionally, by preferentially accumulating near the three-phase contact line, dissolved gases in water are reported to act as line-active agents and increase the magnitude of the line tension promoting nucleation.<sup>21</sup>

Regardless, we acknowledge that the topic of line tension stays controversial in the scientific community. This is mainly due to difficulties in its direct measurability and the wide range of values reported that vary up to a few orders of magnitude and can be both negative and positive.<sup>76</sup> For pure water in hydrophobic nanopores, the reported values are somewhat consistent, ranging from  $-10^{-11}$  J/m to  $-6 \times 10^{-11}$  J/m.<sup>15,36,67,77</sup> The inclusion of line tension necessarily modifies the geometry of the critical nucleus. However, by directly calculating the shape, Guillemot *et al.*<sup>15</sup> found that simply calculating the shape without the line tension and then

adding an energy term proportional to the length of the three-phase contact line is an excellent approximation, which was first hypothesized by Lefevre *et al.*<sup>36</sup> Hence, the only modification to the classical model is to add a line energy term,  $\tau\lambda_c$ , to Eq. (2), where  $\tau$  is the line tension and  $\lambda_c$  is the length of the three-phase contact line of the critical nucleus.<sup>64</sup> We report the theoretical extrusion pressures in Fig. 8 panels (a)–(c) for three different values of line tension: (a)  $\tau = 0$  J/m (i.e., no line tension correction), (b)  $\tau = -1.5 \times 10^{-11}$  J/m, and (c)  $\tau = -3 \times 10^{-11}$  J/m. The orange lines are for the nitrogen–water system, the light blue lines are for the carbon dioxide–water system, and the green lines are for pure water. The required intrusion pressures (the intrusion pressures for a dry pore with no gas or vapor present in the pore) are also shown with black lines as calculated using Eq. (1). The saturation ratios

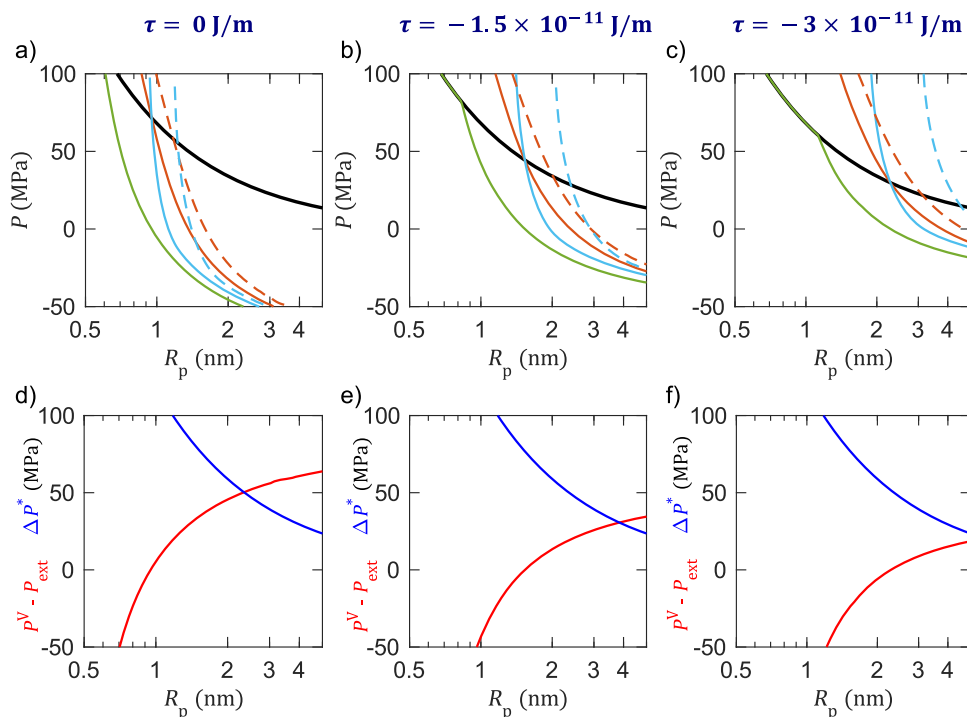


**FIG. 8.** Various pressures of interest as functions of pore radius for different values of line tension: (a) and (d)  $\tau = 0$  J/m, (b) and (e)  $\tau = -1.5 \times 10^{-11}$  J/m, and (c) and (f)  $\tau = -3 \times 10^{-11}$  J/m. The black lines on panels (a)–(c) indicate the intrusion pressures for a dry pore. On these panels, the extrusion pressures are shown in green for pure water, orange for water with dissolved nitrogen, and light blue for water with dissolved carbon dioxide. The solid lines are for  $S = 1$ , and the dashed lines are for  $S = 1.5$ . On panels (d)–(f), the required pressure difference for nucleation,  $P^V - P_{ext}$  (red lines), and the maximum pressure difference where the vapor phase stays confined in the pore after nucleation,  $\Delta P^* = 2\sigma^{LV} \sin \theta_{eq}/R_p$  (blue curves), are shown. All calculations were performed for  $\theta_a = \theta_{eq} = 120^\circ$ ,  $T = 323.15$  K,  $\sigma^{LV} = 0.068$  J/m<sup>2</sup>, and  $\Delta B_c = 35k_B T$ .

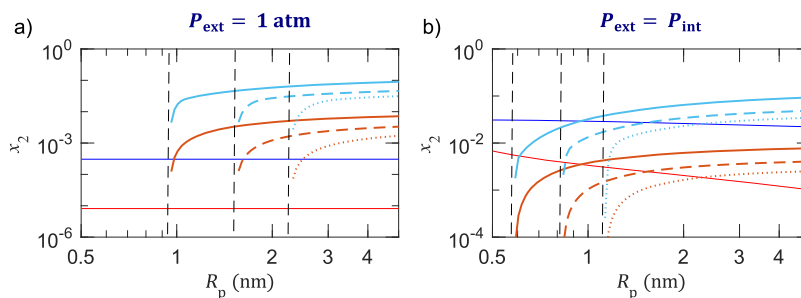


**FIG. 9.** The minimum required gas concentrations in the solution,  $x_2$ , to empty the pore in typical experimental times as functions of pore radius at two different extrusion pressures: (a)  $P_{\text{ext}} = 1 \text{ atm}$  and (b)  $P_{\text{ext}} = P_{\text{int}}$  and for three different values of line tension. The bold solid lines are for  $\tau = 0 \text{ J/m}$ , the dashed lines are for  $\tau = -1.5 \times 10^{-11} \text{ J/m}$ , and the dotted lines are for  $\tau = -3 \times 10^{-11} \text{ J/m}$ . The light blue lines are for carbon dioxide in water, and the orange lines are for nitrogen in water. For reference, the thin, solid blue, and red lines show the saturation concentrations of gases in water at  $P_{\text{ext}}$  for carbon dioxide and nitrogen, respectively. The thin vertical black dashed lines indicate the metastability limit of pure water. All calculations were performed for  $\theta_a = \theta_{\text{eq}} = 120^\circ$ ,  $T = 323.15 \text{ K}$ ,  $\sigma^{\text{LV}} = 0.068 \text{ J/m}^2$ , and  $\Delta B_c = 35k_B T$ .

of gases are  $S = 1$  for the solid curves and  $S = 1.5$  for the dashed curves.

For all cases in Fig. 8 panels (a)–(c), since the amount of dissolved gas decreases as the required intrusion pressure becomes lower with increasing pore size, the effect of the dissolved gas on the nucleation barrier is negligible for large pores. As the pore size gets smaller, however, the effect becomes more pronounced, and below a certain pore size, a filled pore is unstable even at pressures much higher than the required intrusion pressure. Note that this threshold is independent of the type of gas if the saturation ratio is  $S = 1$  but changes with the magnitude of line tension. This is the pore size where a nucleus with zero curvature ( $P^V = P^L$ ) has an energy of  $35k_B T$ , meaning that a fluctuation of this size is enough to empty the pore. Clearly, this pore size is independent of the gas type because we assume that water is saturated with gas at  $P_{\text{int}}$  (i.e., the chemical equilibrium is also at  $P^V = P^L = P_{\text{int}}$ ).

It is seen that the stability of pure water in the pore can be controlled by changing the extrusion pressure for all pore sizes, although the extrusion pressure below a certain pore size becomes at least equal to the intrusion pressure. This is because, at lower temperatures, the pressure of pure water vapor can be taken to be zero because it is small compared to the pressures of interest in the system. Hence, at pressures higher than the intrusion pressure, a filled pore will be stable because the pressure difference required to form a critical nucleus cannot be accommodated in the pore. Once the extrusion pressure is below the intrusion pressure, however, small pores can always accommodate the required pressure difference for chemical equilibrium, while the corresponding nucleus would have an energy barrier  $\Delta B_c \leq 35k_B T$ , resulting in the drying of the pore. For pores larger than a certain size, the extrusion pressure is lower than the intrusion pressure, and this gap grows with the pore size. For pure water at high temperatures (but below the critical temperature), water-filled small pores will be unstable even at pressures significantly higher than the intrusion pressure since the water vapor will have high pressures (i.e., comparable to extrusion pressures). However, the extrusion curve in this region will still be parallel to the intrusion curve. The qualitative differences between the pure-water and the water-with-dissolved-gas cases are the result of water being at subcritical conditions while the dissolved gas is

supercritical. We also note that, between the two gases, the variation of extrusion pressure with pore size is smoother for nitrogen compared to carbon dioxide. This is ultimately due to the differences in the response of gas solubility to pressure variation [see Fig. 9(b), Figs. S2 and S3].

In Fig. 8, panels (d)–(f), we also show the required pressure difference,  $P^V - P_{\text{ext}}$ , in red and the maximum pressure difference a given pore can sustain after nucleation,  $\Delta P^* = 2\sigma^{\text{LV}} \sin \theta_{\text{eq}}/R_p$ , in blue, assuming a flat pore mouth, constant vapor and liquid pressures, and gas concentration after nucleation. With a more negative line tension value, the required pressure difference is not as high, and pores in a larger size range can maintain the confinement of the vapor phase by pinning the liquid–vapor interface [as depicted in Fig. 1(c)].

#### D. Required gas concentration to empty the pore at fixed liquid pressure

Instead of fixing the gas concentration and seeking the required extrusion pressure, the inverse problem can also be solved, which provides more insight. In Fig. 9, the plots of gas concentration vs pore size are given. In panel (a), the extrusion pressure is set to atmospheric pressure, and in panel (b), it is taken to be equal to the intrusion pressure (varying with pore size). On each panel, for each system (orange curves: nitrogen–water; light blue curves: carbon dioxide–water), three curves are shown representing the three different values of line tension. The solid lines are calculated assuming no line tension; the dashed lines are calculated assuming  $\tau = -1.5 \times 10^{-11} \text{ J/m}$ ; and the dotted lines are calculated assuming  $\tau = -3 \times 10^{-11} \text{ J/m}$ . All curves start from a certain pore size below which pure water in the pore becomes unstable (i.e.,  $x_2 = 0$ ; no gas required). These limits are indicated by the vertical dashed lines. We also show the saturation concentration of gases at  $P_{\text{ext}}$  with the solid red (nitrogen–water) and the solid blue (carbon dioxide–water) curves for visual reference. From panel (a), we see that, at atmospheric pressure, the saturation concentrations of these gases are at least a few orders of magnitude lower than what is required for nucleation. On the other hand, from Fig. 9(b), we see that if the liquid is saturated with the gas at the pore intrusion pressure,

there will be a significant shift in what pore sizes can maintain the liquid-filled state. For example, assuming a line tension value of  $\tau = -3 \times 10^{-11}$  J/m, if the liquid is saturated with gas at the intrusion pressure, the pores  $\sim 2.2$  nm or smaller in size are expected to dry, whereas for pure water, this size limit is  $\sim 1.2$  nm [see Fig. 9(b) dotted lines and Fig. 8(c) solid lines].

### E. On the oversolubility and distribution of gas in confinement

So far, we have assumed that the system is homogeneous in terms of the distribution of gas in the bulk and in the pore. However, for pore sizes of interest here (1–5 nm), it is well documented<sup>19,41–47</sup> that the gas tends to migrate into the pores from the bulk resulting in so-called gas oversolubility due to confinement. For example, from molecular simulations,<sup>19</sup> the concentrations of nitrogen and carbon dioxide in water inside a pore size of  $R_p = 1.5$  nm were found to be  $\sim 10$  and  $\sim 5$  times more than the bulk concentration, respectively. Since we consider equilibrium for a vapor nucleus inside the pore and far from the bulk environment, our results are not altered. With oversolubility in mind, when interpreting our results, one should think about the concentrations of gas in the pore and not in the bulk. In practice, this would mean that the amount of gas in the bulk liquid could be an order of magnitude smaller than the saturation concentration (at  $P_{\text{int}}$ ) while still having a significant effect on the extrusion pressure due to oversolubility.

Furthermore, although the distribution of water molecules was found to be bulk-like in the pore, the gas tends to accumulate closer to the walls of the pore.<sup>19,22,23,43</sup> Note that the saturation solubilities of carbon dioxide and nitrogen in water at the conditions considered are  $\sim 5\%$  and  $\sim 0.5\%$  at most, respectively (mole fraction units; see Figs. S2 and S3). If the gas was distributed homogeneously inside the pore, it would be unlikely to get a fluctuation that results in a large vapor nucleus containing  $\sim 10$  gas molecules (corresponding to the typical size of the critical nucleus). The highly localized distribution profile of the gas molecules makes these fluctuations more likely. This further suggests that the nucleus should form near the wall of the pore, where the gas has a significantly higher density.

## VII. COMPARISON WITH AVAILABLE EXPERIMENTAL DATA

We are aware of only one experimental work with open cylindrical nanopores where a large gas volume was dissolved in water, and the drying effects were quantified. In the experiments of Li *et al.*,<sup>25</sup> the authors compared intrusion–extrusion cycles of water in cylindrical nanopores with various amounts of dissolved air. They found that, with more gas present, more of the total pore volume could be recovered at the end of the extrusion process. In these experiments, the samples were not held at high pressures at the end of the intrusion, and the minimum extrusion pressure was atmospheric. We simulated representative experiments by transforming and fitting to the reported pore size distribution data and calculating the corresponding intrusion–extrusion cycles (for analysis of the data and the fitted distribution curve, see the supplementary material). We used nitrogen for calculations assuming that its effect would be very close to that of air. We fixed the temperature and the contact angle at  $T = 298.15$  K and  $\theta_a = \theta_{\text{eq}} = 120^\circ$ , respectively. Note

that these values were not reported in Ref. 25, but the experiments were conducted in lab conditions, and there are other experimental works in the literature<sup>15,36,78</sup> reporting a value of  $\sim 120^\circ$  for the contact angle of pure water with the same grafting/coating material [chloro(dimethyl)octylsilane]. To mimic the experiments, we set the maximum intrusion pressure to 35 MPa. This value corresponds to a minimum intruded pore radius of 2.1 nm, which means that only  $\sim 92\%$  of the total available pore volume,  $\Delta V_{\text{max}}$ , was accessible.

In the experiments of Li *et al.*,<sup>25</sup> they had gas-filled pores as well as a controlled volume of gas at the top of the water column at the beginning of the experiments. During the intrusion, the researchers recorded the pressures at which all extra gas dissolved into the liquid, and for the amount of gas they had, this pressure was always lower than the peak pressure reached in the system. From the information about the pore volume, the calculation of the gas concentration in the pore was straightforward. Then, they calculated the gas concentration in the bulk using the ideal Henry's law and added the extra gas concentration to the pore gas concentration. Since the pore volume and the pressure data are reported in Ref. 25, we could recalculate the extra gas concentration using the nonideal model and determine the gas concentration in the pore more accurately. At the highest gas concentration, we found that our result is  $\sim 16\%$  lower than the reported value calculated with the ideal Henry's law.

The results are summarized in Fig. 10 for  $10^5$  simulated pores (a large number for smoother curves and reproducibility) sampled from the fitted distribution. In panel (a), the simulated intrusion–extrusion cycles are shown. The  $x$ -axis is the normalized volume change of the system,  $\Delta V/\Delta V_{\text{max}}$ , where  $\Delta V$  is the magnitude of the volume change of the system. The black line is the intrusion curve, the green line is the extrusion curve for pure water, and the orange lines are the extrusion curves for water with dissolved nitrogen. The solid orange line is for  $x_2 = 1.518 \times 10^{-3}$ , the dashed orange line is for  $x_2 = 1.055 \times 10^{-3}$ , and the dotted orange line is for  $x_2 = 7.695 \times 10^{-4}$ . These values are the concentrations of nitrogen in the confinement as recalculated here using the data from Ref. 25. In panel (b), the simulated results (blue curve) are compared with the experimental results (green and orange squares) in terms of the percentage of the total intruded pore volume recovered at the end of the extrusion. Note that, in the experiments, the minimum pressure reached at the end of extrusion was atmospheric, which is shown by the horizontal black dashed line in panel (a) (precise value not reported; assumed to be 1 atm). We treated the line tension,  $\tau$ , as an adjustable parameter. A constant value of  $\tau = -4.4 \times 10^{-11}$  J/m was chosen to best fit the experimental data in terms of the root-mean-square deviation from the reported data for the portion of the recovered volume. This value of the line tension is reasonable and within the range of the previously published results for pure water in hydrophobic nanopores.<sup>15,36,67,77</sup>

In Fig. 10(b), it is seen that the simulated line does not exactly go through all experimental points, but it is close and follows a similar trend. One of the main reasons for the deviation could be the accuracy of the reported data and the inherent uncertainties due to the lack of experimental detail. Note that the results in Ref. 25 are given without isolating the volume change purely due to the intrusion and extrusion of solution in and out of the nanopores from other effects, such as the volume change due to

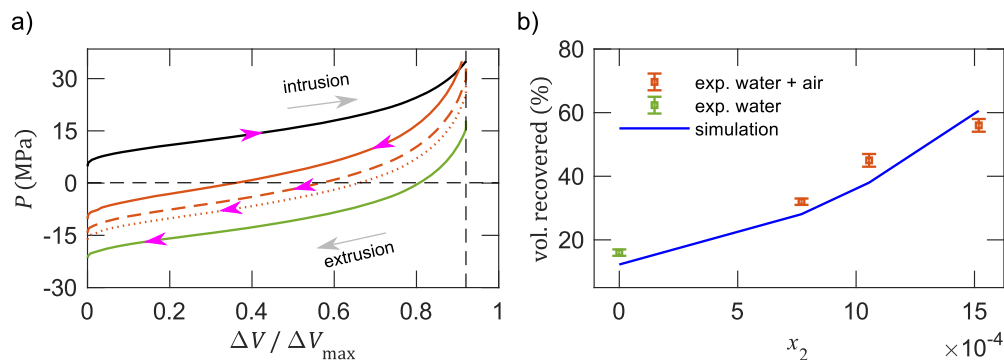


**FIG. 10.** Summary of the simulated experiments based on data from Li *et al.*<sup>25</sup> (a) simulated intrusion–extrusion cycles where the x axis is the magnitude of the normalized volume change of the system,  $\Delta V/\Delta V_{\max}$ . The black line is the intrusion curve, the green line is the extrusion curve for pure water, and the orange lines are the extrusion curves for water with dissolved nitrogen at the recalculated experimental gas concentrations. Note that air was used in the experiments, which is modeled here with nitrogen. The solid orange line is for  $x_2 = 1.518 \times 10^{-3}$ , the dashed orange line is for  $x_2 = 1.055 \times 10^{-3}$ , and the dotted orange line is for  $x_2 = 7.695 \times 10^{-4}$ . The vertical black dashed line shows the maximum intruded volume at peak pressure (0.92). The horizontal black dashed line shows the minimum extrusion pressure in the experiments (1 atm). (b) Comparison of recovered nanopore volume at the end of the experiments when the pressure was brought to 1 atm (green square: pure water, orange squares: water with dissolved air) with the simulated results (blue line). All calculations were performed for  $\theta_a = \theta_{\text{eq}} = 120^\circ$ ,  $T = 298.15$  K,  $\tau = -4.4 \times 10^{-11}$  J/m,  $\sigma^{\text{LV}} = 0.072$  J/m<sup>2</sup>, and  $\Delta B_c = 35k_B T$ . See the main text and the supplementary material for more details.

the compressibility of the test chamber and the compressibility of the solution itself. It is obvious that such effects are important when the intrusion–extrusion cycles in Ref. 25 are compared to other works in the literature where the device was calibrated or the results were numerically corrected like in Ref. 16 (additionally, see the intrusion–extrusion curves in Refs. 36 and 15). Consequently, the way the volume change information was inferred from the raw experimental data is ambiguous. Therefore, we believe that the reported data in Ref. 25 may not exactly reflect the recovered nanopore volume. Clearly, there are other factors and inherent uncertainties, including that the actual macroscopic contact angle could be slightly different than the one we used in the simulations or that the pore size distribution after the hydrophobic coating was applied could be different from the theoretical estimation we made (see the supplementary material). The uncertainties in the ambient temperature and pressure at the time of the experiments are also important, as these parameters are inputs to the phase equilibrium equations. The assumption we made that nitrogen exhibited the same quantitative behavior as air should be reevaluated as well. Additionally, the effects of dissolved gas on the liquid–vapor interfacial tension, the solid–liquid contact angle, and the line tension need to be quantified, which are not considered here. In addition, note that there are uncertainties in selecting  $35k_B T$  as the height of the activation barrier.

## VIII. CONCLUSION

In this paper, we used Gibbsian composite system thermodynamics with classical nucleation theory to study the effects of dissolved nitrogen and carbon dioxide on the behavior of water in hydrophobic cylindrical nanopores open at both ends. For this purpose, we derived an equation relating the nonideal chemical equilibrium of a mixture made of a subcritical solvent and a supercritical gas to the curvature of the liquid–vapor interface. The

role of the confinement geometry on the drying pressure of a nanopore was highlighted. To summarize, in a cylindrical pore, the surface of the energy-minimizing nuclei can be either negatively or positively curved. It is due to this shape that small pores can empty at high liquid pressures. Following previous studies, we used Surface Evolver to calculate the nontrivial nucleus geometry. Unlike previous studies, however, the possibility of symmetric nuclei as part of the nucleation path was ruled out based on physical arguments.

Our findings are in qualitative agreement with the previous molecular dynamics simulations and experiments; that is, the dissolved gas effects are negligible if water is saturated with the gas at atmospheric conditions. However, if, at intrusion pressure, an ample amount of gas is present in the system to dissolve, it can greatly reduce the vapor nucleation barrier and, as a result, increase the pressure at which the pore dries. This was attributed to increased vapor pressure inside the critical nucleus, hence its smaller size and energy compared to the pure-liquid case at the same liquid pressure and temperature. A direct consequence of this is that smaller pores can dry even at pressures much higher than their intrusion pressures (the intrusion pressure for an empty pore). Furthermore, it was found that the ideality assumption typically made in studies of weakly soluble gases may result in significant errors at the conditions of interest.

There is a recent study in the literature where the recovered nanopore volume at the end of extrusion was observed to be proportional to the amount of dissolved air in water. By simulating the experimental intrusion–extrusion cycles and adjusting the line tension, a semi-quantitative agreement could be achieved between the theory and the reported data for water with dissolved air. However, more carefully controlled experiments are needed for a conclusive test of the theory because of the scarcity of available measurements that are directly comparable. Moreover, there are uncertainties in the studied dataset that are difficult to evaluate.

Molecular dynamics simulations might shed light on some of the aspects that are difficult to probe experimentally, such as the concentration of the gas in the pore, the shape of the critical nucleus in the presence of the gas, and phase partitioning during nucleation. Simulation of rare events, such as nucleation, with traditional methods has been difficult and expensive because of the different time scales involved. Up until recently, long waiting times before the onset of nucleation and the fast dynamics near the criticality region have forced researchers to simulate in unrealistic conditions and extrapolate their results. With the development of new, rare-event-specific algorithms and increasing computational power, however, it is becoming feasible to simulate larger systems for longer times obtaining more realistic results.

Finally, we emphasize that what is referred to as line tension in this work is merely an adjustable parameter, and the corresponding energy term scales linearly with the size of the nucleus. In Sec. VII, its value is obtained from fitting to the experimental data. Neither the magnitude nor the sign of this value should be interpreted as the energy of the three-phase contact line, as it empirically accounts for other effects. These other effects include the shortcomings of the continuum approach at the relevant scale, experimental uncertainties (e.g., pore size distribution, temperature), model uncertainties (e.g., the height of the energy barrier), and the simplifications made by neglecting the interfacial effects of the dissolved gas.

## SUPPLEMENTARY MATERIAL

See the supplementary material for the details of the thermodynamic model, the solution procedure for the system of equations, the analytical solution of the symmetric nucleus profile, and the analyzed pore size distribution data from Ref. 25.

## ACKNOWLEDGMENTS

This research was funded by the Natural Sciences and Engineering Research Council (NSERC) of Canada (Grant No. RGPIN-2021-02773). J. A. W. E. holds a Canada Research Chair in Thermodynamics.

## AUTHOR DECLARATIONS

### Conflict of Interest

The authors have no conflicts to disclose.

## Author Contributions

**Hikmat Binyaminov:** Conceptualization (equal); Formal analysis (equal); Investigation (equal); Methodology (equal); Software (equal); Validation (equal); Visualization (equal); Writing – original draft (equal); Writing – review & editing (equal). **Janet A. W. Elliott:** Conceptualization (equal); Formal analysis (equal); Funding acquisition (equal); Investigation (equal); Methodology (equal); Project administration (equal); Resources (equal); Supervision (equal); Validation (equal); Visualization (equal); Writing – review & editing (equal).

## DATA AVAILABILITY

Data sharing is not applicable to this article as no new data were created or analyzed in this study.

## REFERENCES

- 1 A. K. Kota, G. Kwon, W. Choi, J. M. Mabry, and A. Tuteja, *Nat. Commun.* **3**, 1025 (2012).
- 2 V. Eroshenko, R.-C. Regis, M. Soulard, and J. Patarin, *J. Am. Chem. Soc.* **123**, 8129 (2001).
- 3 G. Ortiz, H. Nouali, C. Marichal, G. Chaplais, and J. Patarin, *J. Phys. Chem. C* **118**, 7321 (2014).
- 4 J. Canivet, A. Fateeva, Y. Guo, B. Coasne, and D. Farrusseng, *Chem. Soc. Rev.* **43**, 5594 (2014).
- 5 Y. Grosu, M. Mierzwa, V. A. Eroshenko, S. Pawlus, M. Chorażewski, J.-M. Nedelec, and J.-P. E. Grolier, *ACS Appl. Mater. Interfaces* **9**, 7044 (2017).
- 6 R. Helmy, Y. Kazakevich, C. Ni, and A. Y. Fadeev, *J. Am. Chem. Soc.* **127**, 12446 (2005).
- 7 D. Stoddart, A. J. Heron, E. Mikhailova, G. Maglia, and H. Bayley, *Proc. Natl. Acad. Sci. U. S. A.* **106**, 7702 (2009).
- 8 A. Le Donne, A. Tinti, E. Amayuelas, H. K. Kashyap, G. Camisasca, R. C. Remsing, R. Roth, Y. Grosu, and S. Meloni, *Adv. Phys. X* **7**, 2052353 (2022).
- 9 A. Giacomello, C. M. Casciola, Y. Grosu, and S. Meloni, *Eur. Phys. J. B* **94**, 1 (2021).
- 10 O. Beckstein and M. S. P. Sansom, *Proc. Natl. Acad. Sci. U. S. A.* **100**, 7063 (2003).
- 11 R. Roth, D. Gillespie, W. Nonner, and R. E. Eisenberg, *Biophys. J.* **94**, 4282 (2008).
- 12 S. Rao, C. I. Lynch, G. Klesse, G. E. Oakley, P. J. Stansfeld, S. J. Tucker, and M. S. P. Sansom, *Faraday Discuss.* **209**, 231 (2018).
- 13 G. Hummer, J. C. Rasaiah, and J. P. Noworyta, *Nature* **414**, 188 (2001).
- 14 C. I. Lynch, S. Rao, and M. S. P. Sansom, *Chem. Rev.* **120**, 10298 (2020).
- 15 L. Guillemot, T. Biben, A. Galarneau, G. Vigier, and É. Charlaix, *Proc. Natl. Acad. Sci. U. S. A.* **109**, 19557 (2012).
- 16 L. Guillemot, A. Galarneau, G. Vigier, T. Abensur, and É. Charlaix, *Rev. Sci. Instrum.* **83**, 105105 (2012).
- 17 A. Kopp Lugli, C. S. Yost, and C. H. Kindler, *Eur. J. Anaesthesiol.* **26**, 807 (2009).
- 18 G. Camisasca, A. Tinti, and A. Giacomello, *J. Phys. Chem. Lett.* **11**, 9171 (2020).
- 19 A. Luzar and D. Bratko, *J. Phys. Chem. B* **109**, 22545 (2005).
- 20 Y. Qiao, G. Cao, and X. Chen, *J. Am. Chem. Soc.* **129**, 2355 (2007).
- 21 R. Bey, B. Coasne, and C. Picard, *Proc. Natl. Acad. Sci. U. S. A.* **118**, e2102449118 (2021).
- 22 W. Li, X. Zuo, X. Zhou, and H. Lu, *J. Chem. Phys.* **150**, 104702 (2019).
- 23 K. Leung, A. Luzar, and D. Bratko, *Phys. Rev. Lett.* **90**, 065502 (2003).
- 24 Q. Feng, J. Li, X. Zhou, and H. Lu, *Chin. Phys. B* **31**, 036801 (2022).
- 25 M. Li, L. Xu, and W. Lu, *Langmuir* **36**, 4682 (2020).
- 26 L. Xu, M. Li, and W. Lu, *J. Phys. Chem. C* **125**, 5596 (2021).
- 27 M. Li, C. Zhan, and W. Lu, *Appl. Phys. Lett.* **119**, 181603 (2021).
- 28 L. Zargarzadeh and J. A. W. Elliott, *Langmuir* **35**, 13216 (2019).
- 29 L. Zargarzadeh and J. A. W. Elliott, *Langmuir* **32**, 11309 (2016).
- 30 N. Shardt and J. A. W. Elliott, *J. Phys. Chem. A* **120**, 2194 (2016).
- 31 N. Shardt and J. A. W. Elliott, *J. Phys. Chem. B* **122**, 2434 (2018).
- 32 J. A. W. Elliott, *J. Phys. Chem. B* **124**, 10859 (2020).
- 33 J. A. W. Elliott, *J. Chem. Phys.* **154**, 190901 (2021).
- 34 M. H. Factorovich, V. Molinero, and D. A. Scherlis, *J. Am. Chem. Soc.* **136**, 4508 (2014).
- 35 S. M. A. Malek, P. H. Poole, and I. Saika-Voivod, *J. Chem. Phys.* **150**, 234507 (2019).
- 36 B. Lefevre, A. Saugey, J. L. Barrat, L. Bocquet, E. Charlaix, P. F. Gobin, and G. Vigier, *J. Chem. Phys.* **120**, 4927 (2004).
- 37 B. Lefevre, A. Saugey, J. L. Barrat, L. Bocquet, E. Charlaix, P. F. Gobin, and G. Vigier, *Colloids Surf., A* **241**, 265 (2004).

- <sup>38</sup>N. Giovambattista, A. B. Almeida, S. V. Buldyrev, and A. M. Alencar, *J. Phys. Chem. C* **125**, 5335 (2021).
- <sup>39</sup>C. A. Ward, A. Balakrishnan, and F. C. Hooper, *J. Basic Eng.* **92**, 695 (1970).
- <sup>40</sup>T. W. Forest and C. A. Ward, *J. Chem. Phys.* **66**, 2322 (1976).
- <sup>41</sup>L. N. Ho, Y. Schuurman, D. Farrusseng, and B. Coasne, *J. Phys. Chem. C* **119**, 21547 (2015).
- <sup>42</sup>Y. Hu, L. Huang, S. Zhao, H. Liu, and K. E. Gubbins, *Mol. Phys.* **114**, 3294 (2016).
- <sup>43</sup>M. Pera-Titus, R. El-Chahal, V. Rakotovo, C. Daniel, S. Miachon, and J.-A. Dalmon, *ChemPhysChem* **10**, 2082 (2009).
- <sup>44</sup>L. N. Ho, J. Perez Pellitero, F. Porcheron, and R. J.-M. Pellenq, *Langmuir* **27**, 8187 (2011).
- <sup>45</sup>N. L. Ho, F. Porcheron, and R. J.-M. Pellenq, *Langmuir* **26**, 13287 (2010).
- <sup>46</sup>D. Bratko and A. Luzar, *Langmuir* **24**, 1247 (2008).
- <sup>47</sup>L. N. Ho, S. Clauzier, Y. Schuurman, D. Farrusseng, and B. Coasne, *J. Phys. Chem. Lett.* **4**, 2274 (2013).
- <sup>48</sup>D. Kashchiev, *Nucleation: Basic Theory with Applications* (Butterworth Heinemann, Eastbourne, 2000).
- <sup>49</sup>C. A. Ward and E. Levart, *J. Appl. Phys.* **56**, 491 (1984).
- <sup>50</sup>J. A. W. Elliott and O. Voitcu, *Can. J. Chem. Eng.* **85**, 692 (2007).
- <sup>51</sup>J. A. W. Elliott, *Chem. Eng. Educ.* **35**, 274 (2001), see <https://journals.flvc.org/cee/article/view/122926>.
- <sup>52</sup>L. Zargarzadeh and J. A. W. Elliott, *Langmuir* **29**, 3610 (2013).
- <sup>53</sup>J. R. Elliott and C. T. Lira, *Introductory Chemical Engineering Thermodynamics*, 2nd ed. (Prentice-Hall Inc, Upper Saddle River, 2012).
- <sup>54</sup>H. B. Callen, *Thermodynamics and Introduction to Thermostatistics*, 2nd ed. (John Wiley & Sons, New York, 1985).
- <sup>55</sup>J. J. Carroll, *Chem. Eng. Prog.* **95**, 49 (1999), see <https://www.proquest.com/docview/221523335>.
- <sup>56</sup>F. L. Smith and A. H. Harvey, *Chem. Eng. Prog.* **103**, 33 (2007), see <https://www.nist.gov/publications/avoid-common-pitfalls-when-using-henrys-law>.
- <sup>57</sup>H. Renon and J. M. Prausnitz, *AIChE J.* **14**, 135 (1968).
- <sup>58</sup>D.-Y. Peng and D. B. Robinson, *Ind. Eng. Chem. Fundam.* **15**, 59 (1976).
- <sup>59</sup>R. McGraw, *J. Phys. Chem. B* **105**, 11838 (2001).
- <sup>60</sup>J. S. Beck, J. C. Vartuli, W. J. Roth, M. E. Leonowicz, C. T. Kresge, K. D. Schmitt, C. T. W. Chu, D. H. Olson, E. W. Sheppard, S. B. McCullen, J. B. Higgins, and J. L. Schlenker, *J. Am. Chem. Soc.* **114**, 10834 (1992).
- <sup>61</sup>C. T. Kresge, M. E. Leonowicz, W. J. Roth, J. C. Vartuli, and J. S. Beck, *Nature* **359**, 710 (1992).
- <sup>62</sup>C. Yu, J. Fan, B. Tian, D. Zhao, and G. D. Stucky, *Adv. Mater.* **14**, 1742 (2002).
- <sup>63</sup>K. A. Brakke, *Exp. Math.* **1**, 141 (1992).
- <sup>64</sup>G. G. Poon, "Extending classical nucleation theory: Understanding the effects of trace additives and inhomogeneous concentration distributions," Ph.D. thesis, University of California Santa Barbara, 2018.
- <sup>65</sup>P. K. Bikkina, O. Shoham, and R. Uppaluri, *J. Chem. Eng. Data* **56**, 3725 (2011).
- <sup>66</sup>C. C. M. Luijten and M. E. H. Van Dongen, *J. Chem. Phys.* **111**, 8524 (1999).
- <sup>67</sup>A. Tinti, A. Giacomello, Y. Grosu, and C. M. Casciola, *Proc. Natl. Acad. Sci. U. S. A.* **114**, E10266 (2017).
- <sup>68</sup>R. Giro, P. W. Bryant, M. Engel, R. F. Neumann, and M. B. Steiner, *Sci. Rep.* **7**, 46317 (2017).
- <sup>69</sup>V. Talanquer and D. W. Oxtoby, *J. Chem. Phys.* **114**, 2793 (2001).
- <sup>70</sup>A. Checco, P. Guenoun, and J. Daillant, *Phys. Rev. Lett.* **91**, 186101 (2003).
- <sup>71</sup>F. Staniscia and M. Kanduć, *J. Chem. Phys.* **157**, 184707 (2022).
- <sup>72</sup>C. A. Ward and J. Wu, *Phys. Rev. Lett.* **100**, 256103 (2008).
- <sup>73</sup>M. Barisik and A. Beskok, *Mol. Simul.* **39**, 700 (2013).
- <sup>74</sup>T. Werder, J. H. Walthers, R. L. Jaffe, T. Halicioglu, and P. Koumoutsakos, *J. Phys. Chem. B* **107**, 1345 (2003).
- <sup>75</sup>G. Navascués and P. Tarazona, *J. Chem. Phys.* **75**, 2441 (1981).
- <sup>76</sup>A. Amirfazli and A. W. Neumann, *Adv. Colloid Interface Sci.* **110**, 121 (2004).
- <sup>77</sup>Y. Grosu, O. Ievtushenko, V. Eroshenko, J. M. Nedelec, and J. P. E. Grolier, *Colloids Surf., A* **441**, 549 (2014).
- <sup>78</sup>L. Coiffard and V. Eroshenko, *J. Colloid Interface Sci.* **300**, 304 (2006).

## Supplementary Material for

# “Quantifying the effects of dissolved nitrogen and carbon dioxide on drying pressure of hydrophobic nanopores”

Hikmat Binyaminov, Janet A. W. Elliott\*

Department of Chemical and Materials Engineering, University of Alberta, Edmonton, AB,  
Canada, T6G 1H9

\* Corresponding author: [janet.elliott@ualberta.ca](mailto:janet.elliott@ualberta.ca)

### **This PDF file includes:**

- A. Description of the thermodynamic model
- B. Solution procedure for the system of equations
- C. Analytical solution of the symmetric nucleus profile
- D. Pore size distribution data from Li *et al.*<sup>S31</sup>

## A. Description of the thermodynamic model

### *NRTL activity model*

In the nonrandom two-liquid (NRTL) model,<sup>S1</sup> the activity coefficients are related to the concentration of species through the following equations:

$$\ln \gamma_1 = x_2^2 \left[ \tau_{21} \left( \frac{G_{21}}{x_1 + x_2 G_{21}} \right)^2 + \frac{\tau_{12} G_{12}}{(x_2 + x_1 G_{12})^2} \right] \quad (\text{S1})$$

$$\ln \gamma_2^* = x_1^2 \left[ \tau_{12} \left( \frac{G_{12}}{x_2 + x_1 G_{12}} \right)^2 + \frac{\tau_{21} G_{21}}{(x_1 + x_2 G_{21})^2} \right] - (\tau_{12} + \tau_{21} G_{21}) \quad (\text{S2})$$

with

$$G_{12} = \exp(-\alpha_{12} \tau_{12}) \quad (\text{S3})$$

$$G_{21} = \exp(-\alpha_{21} \tau_{21}) \quad (\text{S4})$$

where  $\alpha_{12}$  and  $\alpha_{21}$  are the nonrandomness parameters. The NRTL interaction parameters,  $\tau_{12}(T)$  and  $\tau_{21}(T)$ , are adjustable parameters in practice that are only functions of temperature.

For carbon dioxide in water, we take  $\alpha_{12} = \alpha_{21} = 0.3$  since it is a polar–nonpolar mixture and use the interaction parameters from Hou *et al.*:<sup>S2</sup>

$$\tau_{12} = 3.720 - \frac{803.18}{T} + 21.13 \left( \frac{T_0 - T}{T} + \ln \frac{T}{T_0} \right) \quad (\text{S5})$$

$$\tau_{21} = 18.664 - \frac{5549.77}{T} - 112.67 \left( \frac{T_0 - T}{T} + \ln \frac{T}{T_0} \right) \quad (\text{S6})$$

where  $T$  (K) is the temperature and  $T_0 = 298.15$  K. Due to its low solubility even at high pressures, for nitrogen in water we use  $\tau_{21} = \tau_{12} = 0$  which means  $\gamma_1 = \gamma_2^* = 1$ .

### *Peng–Robinson EOS*

To calculate the fugacity coefficients in the vapor phase, we use the Peng–Robinson cubic equation of state (P–R EOS).<sup>S3</sup> For the vapor phase of a pure component, it is written as

$$P^V = \frac{\bar{R}T}{v^{\text{PR}} - b^{\text{PR}}} - \frac{a^{\text{PR}}(T)}{v^{\text{PR}}(v^{\text{PR}} + b^{\text{PR}}) + b^{\text{PR}}(v^{\text{PR}} - b^{\text{PR}})} \quad (\text{S7})$$

where  $v^{\text{PR}}$  is the molar volume, and  $a^{\text{PR}}$  and  $b^{\text{PR}}$  are the energy and co-volume parameters defined below:

$$a^{\text{PR}} = \frac{0.457235(\bar{R}T_c)^2\alpha(T)}{P_c} \quad (\text{S8})$$

where  $T_c$  (K) and  $P_c$  (Pa) are the critical temperature and pressure, respectively, and

$$\alpha(T) = \left[ 1 + (0.37464 + 1.54226\omega - 0.26992\omega^2) \left( 1 - \sqrt{\frac{T}{T_c}} \right) \right]^2 \quad (\text{S9})$$

where  $\omega$  is the acentric factor.  $b^{\text{PR}}$  is defined as

$$b^{\text{PR}} = \frac{0.077796\bar{R}T_c}{P_c} \quad (\text{S10})$$

Using mixing rules, the P–R EOS can be extended to mixtures. The classical mixing rules are (written for the vapor phase):<sup>S3,S4</sup>

$$a^{\text{PR}} = \sum_i \sum_j y_i y_j a_{ij}^{\text{PR}} \quad (\text{S11})$$

$$a_{ij}^{\text{PR}} = (1 - k_{ij})\sqrt{a_i a_j} \quad (\text{S12})$$

$$b^{\text{PR}} = \sum_i \sum_j \frac{y_i y_j (b_i + b_j)}{2} \quad (\text{S13})$$

where  $k_{ij}$  is the binary interaction parameter.  $a_i$  and  $b_i$  are the energy and co-volume parameters for pure components, as given by equations (S8) and (S10). By substituting equations (S11) and (S13) into equation (S7), it describes the vapor phase of a mixture.

Equation (S7) is equivalent to solving the following cubic equation<sup>S3</sup>

$$\begin{aligned} Z^3 - (1 - B^{\text{PR}})Z^2 + (A^{\text{PR}} - 3(B^{\text{PR}})^2 - 2B^{\text{PR}})Z \\ - (A^{\text{PR}}B^{\text{PR}} - (B^{\text{PR}})^2 - (B^{\text{PR}})^3) = 0 \end{aligned} \quad (\text{S14})$$

where  $Z$  is the vapor phase compressibility factor defined as

$$Z = \frac{P^V v^{\text{PR}}}{\bar{R}T} \quad (\text{S15})$$

and the parameters  $A^{\text{PR}}$  and  $B^{\text{PR}}$  are defined as

$$A^{\text{PR}} = \frac{a^{\text{PR}} P^V}{(\bar{R}T)^2} \quad (\text{S16})$$

$$B^{\text{PR}} = \frac{b^{\text{PR}} P^V}{\bar{R}T} \quad (\text{S17})$$

Finally, the fugacity coefficients are related to the compressibility and the concentration through the following relation<sup>S3</sup>

$$\begin{aligned} \ln \hat{\phi}_i^V = & \frac{b_i^{\text{PR}}}{b^{\text{PR}}} (Z - 1) - \ln(Z - B^{\text{PR}}) \\ & - \frac{A^{\text{PR}}}{2\sqrt{2}B^{\text{PR}}} \left( \frac{2 \sum_k y_k a_{ki}^{\text{PR}}}{a^{\text{PR}}} \right. \\ & \left. - \frac{b_i^{\text{PR}}}{b^{\text{PR}}} \right) \ln \left[ \frac{Z + (1 + \sqrt{2})B^{\text{PR}}}{Z + (1 - \sqrt{2})B^{\text{PR}}} \right] \end{aligned} \quad (\text{S18})$$

where  $\hat{\phi}_i^V$  is the fugacity coefficient of component  $i$  in the vapor phase. The required parameters for the systems of interest in this work are given in Table S1.<sup>S5</sup>

**Table S1. Parameters for P-R EOS calculations.**<sup>S5</sup>

component	$T_c$ (K)	$P_c$ (MPa)	$\omega$

water	647.10	22.064	0.3443
nitrogen	126.19	3.3958	0.0372
carbon dioxide	304.13	7.3773	0.2239

We use constant (temperature-independent) interaction parameters from Soreide *et al.*<sup>S6</sup> for both systems:  $k_{\text{H}_2\text{O}-\text{N}_2} = 0.4778$  and  $k_{\text{H}_2\text{O}-\text{CO}_2} = 0.1896$ .

Calculating  $\phi_{1,\text{sat}}$ ,  $H_{12}$ ,  $\bar{v}_{2,\infty}^L$ ,  $P_{1,\text{sat}}$ , and  $v_{1,\text{sat}}^L$

To calculate the fugacity coefficient of the vapor of pure water at saturation,  $\phi_{1,\text{sat}}$ , we use the correlation from Hass:<sup>S7</sup>

$$\phi_{1,\text{sat}} = \exp\left(\frac{10P_{1,\text{sat}}p_0 + 5P_{1,\text{sat}}^2\bar{T}^6p_1 + 2P_{1,\text{sat}}^5\bar{T}^{24}p_2}{46.151T}\right) \quad (\text{S19})$$

with

$$p_0 = 0.512004 - 1.191807\bar{T} + 2.599832\bar{T}^2 - 21.433083\bar{T}^3 + 15.281761\bar{T}^4 - 2.527165\bar{T}^5 - 2.454047\bar{T}^6 \quad (\text{S20})$$

$$p_1 = 0.661366 - 3.258346\bar{T} + 6.393115\bar{T}^2 - 6.447504\bar{T}^3 + 3.202128\bar{T}^4 - 0.514945\bar{T}^5 - 0.120192\bar{T}^6 \quad (\text{S21})$$

$$\begin{aligned}
p_3 = & (8.44104 + 28.86344\bar{T} - 270.10366\bar{T}^2 + 624.08835\bar{T}^3 \\
& - 675.70455\bar{T}^4 + 363.16788\bar{T}^5 - 79.26405\bar{T}^6) \quad (S22) \\
& \times 10^{-6}
\end{aligned}$$

where  $T$  (K) is the temperature and  $\bar{T} = T/500$ .

We calculate the Henry's law constant,  $H_{12}$ , for nitrogen in water from the correlation of Harvey<sup>S8</sup> using the improved parameters of Prini *et al.*<sup>S9</sup> (given in units of Pa):

$$\begin{aligned}
H_{12} = \exp\left(-\frac{9.67578}{T_r} + 4.72162 \frac{(1 - T_r)^{0.355}}{T_r} \right. \\
\left. + 11.70585 T_r^{-0.41} \exp(1 - T_r)\right) P_{1,\text{sat}} \quad (S23)
\end{aligned}$$

where  $T$  (K) is the temperature,  $P_{1,\text{sat}}$  (Pa) is the saturation vapor pressure of pure water at  $T$ , and  $T_r = T/647.1$ .

We calculate the Henry's law constant,  $H_{12}$ , for carbon dioxide in water using the correlation of Hou *et al.*<sup>S2</sup> (given in units of Pa):

$$\begin{aligned}
H_{12} = 10^6 \exp\left(-6.1384 + 42.842 \left(\frac{T_0}{T}\right) - 44.358 \left(\frac{T_0}{T}\right)^2 \right. \\
\left. + 12.786 \left(\frac{T_0}{T}\right)^3\right) \quad (S24)
\end{aligned}$$

where  $T$  (K) is the temperature and  $T_0 = 298.15$  K.

We find the infinite dilution partial molar volume of nitrogen in water,  $\bar{v}_{2,\infty}^L$ , from the correlation of Sun<sup>S10</sup> (given in units of m<sup>3</sup>/mol):

$$\begin{aligned}\bar{v}_{2,\infty}^L = \bar{R} & \left( 2.3546047 \times 10^{-5} - 1.04544 \times 10^{-14} P^L \right. \\ & - 4.3078 \times 10^{-7} T - 8.09187 \times 10^{-7} \frac{T}{680 - T} \\ & \left. + 6.474123 \times 10^{-8} T \ln T \right) \quad (\text{S25})\end{aligned}$$

where  $T$  (K) is the temperature and  $P^L$ (Pa) is the liquid pressure.

For carbon dioxide in water, we calculate the infinite dilution partial molar volume of the gas using the correlation of Sedlbauer *et al.*<sup>S11</sup> (given in units of m<sup>3</sup>/mol):

$$\begin{aligned}\bar{v}_{2,\infty}^L = \kappa_{T,1} \bar{R} T + 0.5558 (v_1^L - \kappa_{T,1} \bar{R} T) \\ + \kappa_{T,1} \bar{R} T \rho_1 \left( 3.3921 \times 10^{-3} \right. \\ - 1.3880 \times 10^{-5} \exp\left(\frac{1500}{T}\right) \\ + 1.4801 \times 10^{-4} [\exp(0.005\rho_1) - 1] \\ \left. + 1.2 \times 10^{-3} [\exp(-0.01\rho_1) - 1] \right) \quad (\text{S26})\end{aligned}$$

where  $\kappa_{T,1}$  (Pa<sup>-1</sup>) is the isothermal compressibility,  $v_1^L$  (m<sup>3</sup>/mol) is the molar volume, and  $\rho_1$ (kg/m<sup>3</sup>) is the mass density of pure liquid water at  $T$  (K) and  $P^L$  (Pa). The values of  $\kappa_{T,1}$ ,  $v_1^L$ , and  $\rho_1$  as well as the saturation properties,  $P_{1,\text{sat}}$  and  $v_{1,\text{sat}}^L$ , for water are taken from REFPROP 10.<sup>S5</sup> Note that, for ease of reference, we generated look-up tables using

REFPROP 10<sup>S5</sup> for the properties of interest at each temperature used in our work. In these tables, we set the pressure increment to 0.1 MPa and used linear interpolation for in-between values.

The plots of molar volumes as functions of pressure at three different temperatures are given in Figure S1. In all cases, the linear (or close to linear) dependence on pressure allows us to evaluate the molar volume integrals in the phase equilibrium equations (equations (13) and (22)) by the trapezoidal rule:  $\int_a^b f(x)dx \approx (f(a) + f(b))(b - a)/2$  without loss of accuracy.

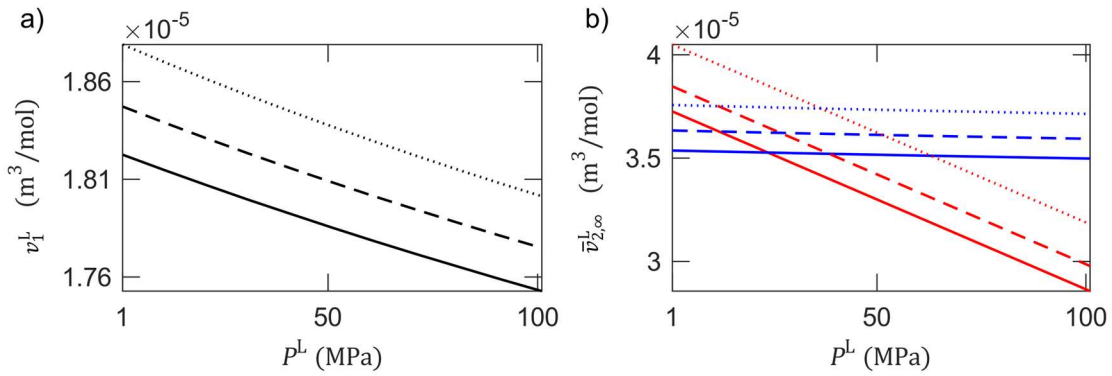


**Figure S1.** Plots of molar volumes as functions of pressure at three different temperatures:  $T = 323.15$  K (solid lines),  $T = 348.15$  K (dashed lines), and  $T = 373.15$  K (dotted lines). Panel (a) shows the plots of pure liquid water molar volume,  $v_1^l$ , and panel (b) shows the plots of infinite dilution partial molar volume,  $\bar{v}_{2,\infty}^l$ , for nitrogen in water (red lines) and for carbon dioxide in water (blue lines).

#### *Validation of the thermodynamic model*

We plot the mutual solubilities of nitrogen–water and carbon dioxide–water systems at three different temperatures and at high pressures (up to 100 MPa) in Figure S2 and Figure S3, respectively, as calculated from the (nonideal) model described in this work. Some experimental data points from the literature are also shown for comparison. Overall,

although it is relatively simple, the model captures the behaviour of both systems in the entire pressure range accurately enough for our purposes.

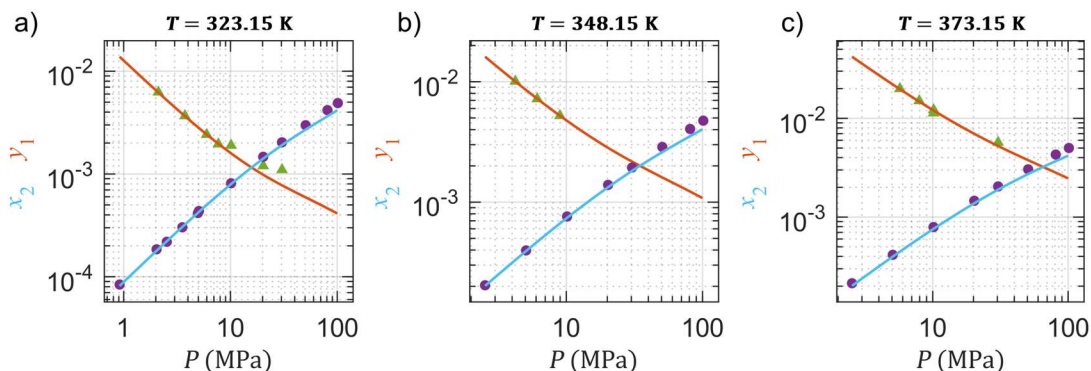


**Figure S2. Mutual solubilities of nitrogen and water as functions of pressure at three different temperatures: (a)  $T = 323.15$  K, (b)  $T = 348.15$  K, and (c)  $T = 373.15$  K. The orange lines show the mole fraction of water in vapor phase,  $y_1$ , and light blue lines show the mole fraction of nitrogen in the liquid phase,  $x_2$ , as calculated from the model described in this work. The green markers are the experimental data points for the water concentration in the vapor phase and violet markers are the experimental data points for the gas concentration in the liquid phase from the literature<sup>S12–S15</sup> as compiled in reference<sup>S16</sup>.**

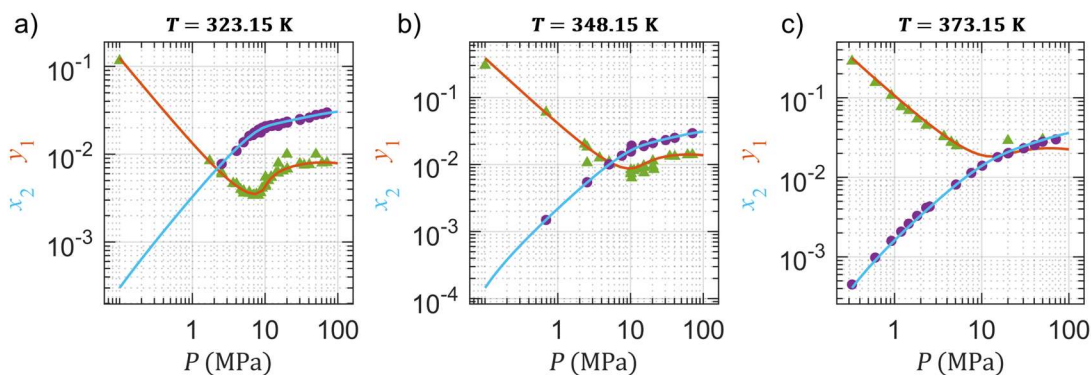


**Figure S3. Mutual solubilities of carbon dioxide and water as functions of pressure at three different temperatures: (a)  $T = 323.15$  K, (b)  $T = 348.15$  K, and (c)  $T = 373.15$  K. The orange lines show the mole fraction of water in the vapor phase,  $y_1$ , and the light blue lines show the mole fraction of carbon dioxide in the liquid phase,  $x_2$ , as calculated from the model described in this work. The green markers are the experimental data points for the water concentration in the vapor phase and the violet markers are the experimental data points for the gas concentration in the liquid phase from the literature<sup>S17–S28</sup> as compiled in reference<sup>S29</sup>.**

## B. Solution procedure for the system of equations

In general, at a fixed temperature, there are eleven equations that need to be solved simultaneously for thermodynamic equilibrium:

$$\left\{ \begin{array}{l}
\text{equation (12)} \\
\text{equation (21)} \\
\text{equation (S14)} \\
x_1 + x_2 = 1 \\
y_1 + y_2 = 1 \\
\gamma_1 = \gamma_1(x_1, x_2) \\
\gamma_2^* = \gamma_2^*(x_1, x_2) \\
\hat{\phi}_1^V = \hat{\phi}_1^V(P^V, Z, y_1, y_2) \\
\hat{\phi}_2^V = \hat{\phi}_2^V(P^V, Z, y_1, y_2) \\
v_1^L = v_1^L(P^L) \\
\bar{v}_{2,\infty}^L = \bar{v}_{2,\infty}^L(P^L)
\end{array} \right. \quad (\text{S27})$$

There are thirteen unknowns:  $P^L$ ,  $P^V$ ,  $Z$ ,  $x_1$ ,  $x_2$ ,  $y_1$ ,  $y_2$ ,  $\hat{\phi}_1^V$ ,  $\hat{\phi}_2^V$ ,  $\gamma_1$ ,  $\gamma_2^*$ ,  $v_1^L$ , and  $\bar{v}_{2,\infty}^L$ . This means that two more equations are required to close the system of equations. We have four cases that are relevant in this work:

- a) to solve for saturation across a flat interface

Step 1. fix the system pressure at  $P^L = P^V = \text{constant}$  (when pressure is known) or fix the gas concentration at  $x_2 = \text{constant}$  and set  $P^L = P^V$  (when concentration is known)

Step 2. solve the system of equations (S27)

- b) to find the free energy barrier for the given pore size at fixed gas concentration and liquid pressure

Step 1. fix the gas concentration at  $x_2 = \text{constant}$  and the liquid pressure at  $P^L = \text{constant}$

Step 2. find the vapor pressure,  $P^V$ , by solving the system of equations (S27)

Step 3. find the curvature,  $k_c$ , of the corresponding shape using equation (7)

(or equation 23)

- Step 4. find the shape and its energy,  $\Delta B_c$ , for the prescribed curvature and pore radius by interpolating in the geometry data from Surface Evolver
- c) to find the extrusion pressure for the given pore size at fixed gas concentration
- Step 1. fix the gas concentration at  $x_2 = \text{constant}$  and take the free energy barrier to be  $\Delta B_c = 35k_B T$
- Step 2. find the corresponding nucleus curvature,  $k_c$ , by interpolating in the geometry data from Surface Evolver for the specified pore radius
- Step 3. use equation (7) to find  $P^V - P^L = \text{constant}$
- Step 4. solve the system of equations (S27) to find  $P_{\text{ext}} = P^L$
- d) to find the required gas concentration to empty a given pore at fixed liquid pressure
- Step 1. fix the liquid pressure  $P^L = P_{\text{ext}} = \text{constant}$  and take the free energy barrier to be  $\Delta B_c = 35k_B T$
- Step 2. find the corresponding nucleus curvature,  $k_c$ , by interpolating in the geometry data from Surface Evolver for the specified pore radius
- Step 3. use equation (7) to determine the vapor pressure,  $P^V$
- Step 4. solve the system of equations (S27) to find the gas concentration,  $x_2$

The system of equations (S27) is solved numerically in MATLAB (v. 2021a, Natick, MA, USA) using the built-in solver *vpasolve()* by providing physically appropriate ranges for the variables. The pressure dependence of the molar volume of pure water and the partial molar volume of carbon dioxide is implicit and complicated. However, they are much weaker functions of pressure compared to the partial molar volume of nitrogen (see Figure S1). If the liquid pressure is an unknown that is to be found by solving the system of

equations (*e.g.*, extrusion pressure calculations; see (c) above), the molar volume of water and the partial molar volume of carbon dioxide are fixed at  $P_{1,\text{sat}}$  as constants. For the nitrogen–water system, since  $\bar{v}_{2,\infty}^L$  is explicitly given as a linear function of pressure, only water molar volume is fixed at  $P_{1,\text{sat}}$ .

### C. Analytical solution of the symmetric nucleus profile

It is possible to develop an analytical solution for the shape of the critical nucleus by requiring it to have rotational symmetry with the axis of symmetry being the cylinder axis and solving the variational problem (*i.e.*, the Euler–Lagrange equation). This solution is given by Lefevre *et al.*<sup>S30</sup> and the final equation for the profile is (translated to our notation)

$$d(r) = \pm \int_a^r \frac{2\cos\theta_{\text{eq}} + R_p k_c (x^2 - 1)}{\sqrt{4x^2 - (2\cos\theta_{\text{eq}} + R_p k_c (x^2 - 1))^2}} dx \quad (\text{S28})$$

where the magnitude of  $d(r)$  is the distance to the liquid–vapor interface from a circle of radius  $r$  on the radial plane whose center is on the cylinder axis.  $x$  is an integration variable, and the lower bound of integration,  $a$ , is given as

$$a = \frac{\sqrt{1 - R_p k_c (2\cos\theta_{\text{eq}} - R_p k_c)} - 1}{R_p k_c} \quad (\text{S29})$$

Equation (S28) is integrated numerically. Example profiles calculated using equation (S28) are shown in Figure 3c.

#### D. Pore size distribution data from Li *et al.*<sup>S31</sup>

The normalized pore volume distribution data from Li *et al.*<sup>S31</sup> is given in Figure S4a (manually digitized) for which the reported volume-based mean is 6 nm. We converted this data to a number distribution by dividing each data point by  $\pi R_p^2 l_p$  where  $l_p$  is the pore length assumed to be a constant (independent of  $R_p$ ). This distribution data is for the raw hydrophilic material as received. To make the pores hydrophobic, the pore surfaces were coated with a thin layer of chloro(dimethyl)octylsilane. Although the authors do not mention the pore size distribution after this step, we could estimate the thickness of the applied layer using the method of Fadeev *et al.*<sup>S32</sup> Due to the structural differences in the arrangement of the molecules in this layer, the layer thickness is about one third of the radius for pores smaller than  $\sim 2.5$  nm in radius and  $\sim 1$  nm for larger pores. In order to have a continuous variation, we chose a slightly higher cut-off value at  $R_p = 3$  nm and subtracted the layer thickness from the pore radii.

After transforming the data, we fitted a continuous distribution curve to this data using MATLAB's built-in distribution fitter *fitdist()*. This function fits a chosen distribution to data using maximum likelihood estimation. Among many common distribution types tried, the Weibull distribution fitted the data best (*i.e.*, the lowest root-mean-square deviation) with the number-based mean of  $2.5 \times 10^{-9}$  m and the variance of  $3.1 \times 10^{-18}$  m<sup>2</sup>. The fitted curve is shown in Figure S4b (black line) together with the transformed data. Using the fitted distribution, we could generate a collection of pores mimicking the samples in the experiments and simulate the intrusion–extrusion curves.

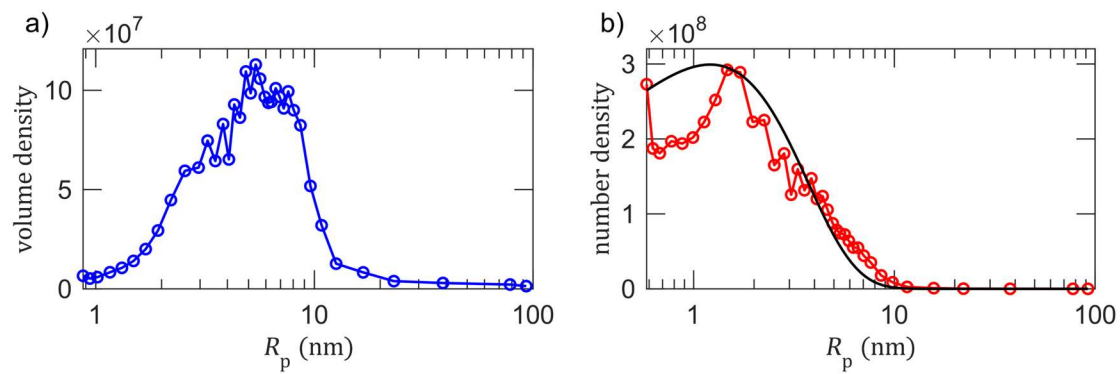


**Figure S4. Pore size distribution data from the work of Li *et al.*<sup>S31</sup> (a) volume density data as originally reported but normalized, (b) transformed number density data with hydrophobic layer thickness subtracted (red) and fitted with continuous distribution curve (black line). All curves (both data curves and the fitted curve) are normalized in the data range to unity.**

- <sup>S1</sup> H. Renon and J.M. Prausnitz, *AIChE J.* **14**, 135 (1968).
- <sup>S2</sup> S.X. Hou, G.C. Maitland, and J.P.M. Trusler, *J. Supercrit. Fluids* **73**, 87 (2013).
- <sup>S3</sup> D. Peng and D.B. Robinson, *Ind. Eng. Chem. Fundam.* **15**, 59 (1976).
- <sup>S4</sup> J.M. Prausnitz, R.N. Lichtenthaler, and E.G. de Azevedo, *Molecular Thermodynamics of Fluid-Phase Equilibria*, 3rd ed. (Prantice Hall PTR, Upper Saddle River, NJ, 1999).
- <sup>S5</sup> E.W. Lemmon, I.H. Bell, M.L. Huber, and M.O. McLinden, (2018).
- <sup>S6</sup> I. Søreide and C.H. Whitson, *Fluid Phase Equilib.* **77**, 217 (1992).
- <sup>S7</sup> J.L. Hass, *Geochim. Cosmochim. Acta* **34**, 929 (1970).
- <sup>S8</sup> A.H. Harvey, *AIChE J.* **42**, 1491 (1996).
- <sup>S9</sup> R. Fernández-Prini, J.L. Alvarez, and A.H. Harvey, *J. Phys. Chem. Ref. Data* **32**, 903 (2003).
- <sup>S10</sup> R. Sun, W. Hu, and Z. Duan, *J. Solution Chem.* **30**, 561 (2001).
- <sup>S11</sup> J. Sedlbauer, J.P. O'Connell, and R.H. Wood, *Chem. Geol.* **163**, 43 (2000).
- <sup>S12</sup> R. Wiebe, V.L. Gaddy, and C. Heins, *J. Am. Chem. Soc.* **55**, 947 (1933).
- <sup>S13</sup> M. Rigby and M. Prausnitz, *J. Phys. Chem.* **72**, 330 (1968).
- <sup>S14</sup> A. Chapoy, A.H. Mohammadi, B. Tohidi, and D. Richon, *J. Chem. Eng. Data* **49**, 1110 (2004).
- <sup>S15</sup> A.W. Saddington and N.W. Krase, *J. Am. Chem. Soc.* **56**, 353 (1934).
- <sup>S16</sup> A.M. Abudour, S.A. Mohammad, and K.A.M. Gasem, *Fluid Phase Equilib.* **319**, 77 (2012).
- <sup>S17</sup> R. Wiebe and V.L. Gaddy, *J. Am. Chem. Soc.* **61**, 315 (1939).
- <sup>S18</sup> R. Wiebe and V.L. Gaddy, *J. Am. Chem. Soc.* **63**, 475 (1941).
- <sup>S19</sup> R. Dohrn, A.P. Büinz, F. Devlieghere, and D. Thelen, *Fluid Phase Equilib.* **83**, 149 (1993).
- <sup>S20</sup> A. Bamberger, G. Sieder, and G. Maurer, *J. Supercrit. Fluids* **17**, 97 (2000).
- <sup>S21</sup> C.R. Coan and A.D. King, *J. Am. Chem. Soc.* **93**, 1857 (1971).

- <sup>S22</sup> K. Tödheide and E.U. Franck, *Zeitschrift Für Phys. Chemie* **37**, 387 (1963).
- <sup>S23</sup> K. Jackson, L.E. Bowman, and J.L. Fulton, *Anal. Chem.* **67**, 2368 (1995).
- <sup>S24</sup> G. Müller, E. Bender, and G. Maurer, *Berichte Der Bunsengesellschaft Für Phys. Chemie* **92**, 148 (1988).
- <sup>S25</sup> P.C. Gillespie and G.M. Wilson, *Vapor–Liquid and Liquid–Liquid Equilibria: Water–Methane, Water–Carbon Dioxide, Water–Hydrogen Sulfide, Water–NPentane, Water–Methane–NPentane. Research Report RR-48* (Gas Processors Association, Tulsa, OK, 1982).
- <sup>S26</sup> J.A. Briones, J.C. Mullins, and M.C. Thies, *Fluid Phase Equilib.* **36**, 235 (1987).
- <sup>S27</sup> R. D’Souza, J.R. Patrick, and A.S. Teja, *Can. J. Chem. Eng.* **66**, 319 (1988).
- <sup>S28</sup> T. Sako, T. Sugeta, N. Nakazawa, T. Okubo, M. Sato, T. Taguchi, and T. Hiaki, *J. Chem. Eng. Japan* **24**, 449 (1991).
- <sup>S29</sup> N. Spycher, K. Pruess, and J. Ennis-King, *Geochim. Cosmochim. Acta* **67**, 3015 (2003).
- <sup>S30</sup> B. Lefevre, A. Saugey, J.L. Barrat, L. Bocquet, E. Charlaix, P.F. Gobin, and G. Vigier, *J. Chem. Phys.* **120**, 4927 (2004).
- <sup>S31</sup> M. Li, L. Xu, and W. Lu, *Langmuir* **36**, 4682 (2020).
- <sup>S32</sup> A.Y. Fadeev and S.M. Staroverov, *J. Chromotography A* **447**, 103 (1988).